

PENCO: A Physics–Energy–Numerical-Consistent Operator for 3D Phase Field Modeling

Mostafa Bamdad*¹ | Mohammad Sadegh Eshaghi†² | Cosmin Anitescu² | Navid Valizadeh² | Timon Rabczuk‡¹

¹ Chair of Computational Mechanics, Institute of Structural Mechanics, Bauhaus-Universität Weimar, 99423 Weimar, Germany

² Chair of Computational Science and Simulation Technology, Institute of Photonics, Department of Mathematics and Physics, Leibniz University Hannover, 30167 Hannover, Germany

Abstract

Accurate and efficient solutions of spatio-temporal partial differential equations (PDEs), such as phase-field models, are fundamental for understanding interfacial dynamics and microstructural evolution in materials science and fluid mechanics. Neural Operators (NOs) have recently emerged as powerful data-driven alternatives to traditional solvers; however, existing architectures often accumulate temporal errors, struggle to generalize in long-horizon simulations, and require large training datasets. To overcome these limitations, we propose PENCO (Physics–Energy–Numerical–Consistent Operator), a hybrid operator-learning framework that seamlessly integrates physical laws and numerical structure within a data-driven architecture. The formulation introduces an enhanced L^2 Gauss–Lobatto collocation residual around the temporal midpoint that robustly enforces the governing dynamics and significantly improves accuracy, a Fourier-space numerical consistency term that captures the balanced behavior of semi-implicit discretizations, and an energy-dissipation constraint that ensures thermodynamic consistency. Additional low-frequency spectral anchoring and teacher-consistency mechanisms further stabilize learning and suppress long-term error growth. This hybrid design enables PENCO to preserve governing physics while mitigating long-term error growth. Through extensive three-dimensional phase-field benchmarks covering phase ordering, crystallization, epitaxial growth, and complex pattern formation, PENCO demonstrates superior accuracy, stability, and data efficiency compared to state-of-the-art neural operators, including Multi-Head Neural Operator (MHNO) and Fourier Neural Operator (FNO-4D), while maintaining physically consistent evolution. The associated dataset and implementation are available at github.com/MBamdad/PENCO.

Keywords: | Phase Field Systems | Neural Operators | Physics-Guided Learning | PENCO | Multi-Head Neural Operator | Fourier Neural Operator | Semi-Implicit Consistency | Energy Dissipation | 3D Spatio-Temporal Modeling

* Corresponding author. Email: mostafa.bamdad@uni-weimar.de

† Corresponding author. Email: eshaghi.khanghah@iop.uni-hannover.de

‡ Corresponding author. Email: timon.rabczuk@uni-weimar.de

1 Introduction

Partial differential equations (PDEs) [1] provide the mathematical foundation for modeling systems that evolve in space and time, capturing complex dynamics in disciplines like fluid flow [2], heat transfer [3], and structural mechanics [4]. A particularly important class of these models is three-dimensional phase-field equations [5], which include formulations for Allen Cahn (AC), Cahn Hilliard (CH), Swift Hohenberg (SH), Phase Field Crystal (PFC), and Molecular Beam Epitaxy (MBE) growth [6, 7]. These equations are powerful tools for simulating interfacial dynamics and material evolution. By using smoothly varying order parameters to represent distinct material phases, they are used to handle problems with complex topological changes, such as crack evolution, boiling, and multiphase flows [6, 8-10]. Consequently, they have become indispensable in studying phenomena such as solidification [11], microstructure evolution [12], and phase separation [13].

Traditional numerical solvers such as finite difference [14] and finite element methods [15, 16] have been extensively used to solve these systems. However, their computational cost can be prohibitive for large-scale or repeated simulations required in design optimization, uncertainty quantification, and inverse analysis [17].

In recent years, machine learning has emerged as a transformative paradigm for accelerating the solution of PDE-governed systems. These approaches can be broadly categorized into three classes. The first are data-driven models, such as NOs [18-24], which learn mappings between function spaces directly from simulation data. The second are physics-driven methods, notably Physics-Informed Neural Networks (PINNs) [25-29], which embed governing physical laws into the loss function. The third are hybrid physics-informed operator-learning frameworks [30-34], which combine the generalization capability of NOs with the physical interpretability of PINNs.

Purely data-driven approaches such as the FNO [35], DeepONet [22, 36], and Graph Neural Operators [37] have achieved remarkable success in modeling complex systems, including phase-field dynamics [38]. Nevertheless, these architectures often require large, high-fidelity datasets, lack embedded physical constraints, and may suffer from overfitting and poor extrapolation [39-41]. Conversely, PINNs mitigate data dependency by incorporating PDE residuals into their loss function [29], enabling physically consistent predictions. This principle has been successfully applied to challenging problems in solid mechanics, such as the analysis of functionally graded porous beams [42], demonstrating the potential of physics-informed learning in engineering contexts. Despite these advantages, standard PINNs struggle with the stiff, multiscale nature of phase-field equations [43] and exhibit limited generalization across varying initial conditions [44], frequently requiring costly retraining [45-47].

To bridge this gap, physics-informed operator-learning methods have emerged as a promising solution, combining the expressivity of NOs with the physical grounding of PINNs. For instance, the PINO enhances an FNO by incorporating PDE residuals into the loss function, enabling it to achieve high accuracy with fewer data points [30]. This field is rapidly evolving, with ongoing research into the most effective ways to integrate physical laws. Some methods employ adaptive weighting between data and physics losses

[48], while recent innovations like the variational physics informed neural operator (VINO) propose minimizing an energy based variational form of the PDE. This latter approach can improve training efficiency and accuracy, particularly on fine discretizations, by avoiding the direct computation of high order derivatives [49].

While these developments mark significant progress, most operator-learning frameworks still face difficulties in modeling stiff spatiotemporal systems with long temporal horizons. Architectures such as FNO-3D [36] and Phase-Field DeepONet [31] typically employ autoregressive strategies, predicting one or a few time steps at a time. This approach introduces cumulative error and instability in long-time predictions. The FNO-4D partially alleviates this by treating time as an additional input channel, enabling simultaneous learning of spatiotemporal correlations. However, its design lacks explicit causal coupling between consecutive time steps, which is fundamental for physical consistency.

The MHNO [50] was introduced to address the challenges of autoregressive error accumulation and non-causal temporal prediction. Its projection-based temporal mechanism enforces causality while enabling the prediction of all time steps in a single forward pass, resulting in improved temporal coherence and numerical stability compared to purely recurrent or fully parallel designs. However, despite these architectural advantages, MHNO remains fundamentally data-driven and exhibits a strong dependence on large, high-quality datasets for accurate generalization. In data-limited regimes, its prediction error tends to accumulate over time, and the model shows degraded accuracy for unseen initial conditions due to the absence of embedded physical constraints. Consequently, while MHNO enhances temporal connectivity, it does not inherently ensure physical consistency or data efficiency.

Building on these advances, the present work introduces PENCO (Physics-Energy-Numerical-Consistent Operator), a new hybrid framework that combines data efficiency, physical fidelity, and numerical stability within a single operator-learning model. Instead of simply augmenting existing neural operators with residual penalties, PENCO is designed around a principled integration of how physics and numerics interact during temporal evolution. Its learning process mimics the structure of semi-implicit solvers by balancing explicit nonlinear updates with spectrally preconditioned linear components, thereby achieving the stability of classical numerical schemes within a trainable neural framework. The model learns from both data and physics simultaneously, guided by collocation-based constraints that maintain temporal coherence and by energy-based regularization that enforces thermodynamic admissibility.

In addition, PENCO stabilizes large-scale structures through a spectral anchoring mechanism that preserves low-wavenumber dynamics while allowing fine-scale features to adaptively evolve. This hybrid formulation captures the essential physical invariants of phase-field systems and suppresses the error accumulation that typically plagues long-horizon operator learning. As a result, PENCO generalizes across different physical regimes and maintains numerical consistency comparable to advanced semi-implicit solvers, bridging the gap between traditional computation and modern data-driven modeling.

The remainder of this study is organized as follows: [Section 2](#) details the methodologies, providing an overview of the FNO-4D, MHNO, and the proposed PENCO frameworks. [Section 3](#) details the data

generation procedure and training–budget protocol adopted to assess model performance under data-scarce conditions. [Section 4](#) presents the computational experiments on several 3D phase field equations, including the AC, CH, SH, PFC, and MBE models. Finally, [Section 5](#) concludes the paper with a summary of the findings and potential directions for future research.

2 Methodology

This section presents the operator-learning frameworks used to model three-dimensional phase-field dynamics. We first summarize the baseline architectures used for comparison, namely the FNO-4D adapted to four-dimensional spatiotemporal inputs and the MHNO. We then introduce PENCO, which builds upon a spectral neural-operator backbone but fundamentally changes the training objective by embedding physical laws and numerical structure into the learning process. All models are trained to approximate the solution operator of phase-field-type PDEs of the form $\partial_t u = \mathcal{N}(u, \nabla u, \nabla^2 u, \dots)$, where \mathcal{N} is a nonlinear differential operator. The operator maps an initial to the full spatiotemporal evolution of the field.

2.1 Operator-Learning Setting

Let $\Omega \in \mathbb{R}^3$ denotes a periodic spatial domain, $t \in [0, T]$ the time interval, and

$$u(\mathbf{x}, t): \Omega \times [0, T] \rightarrow \mathbb{R} \quad (1)$$

a scalar order parameter governed by a phase-field equation. In an operator-learning setting, we seek to approximate the solution operator

$$\mathcal{G}_\theta: a(\mathbf{x}) \mapsto u(\mathbf{x}, t), \quad (2)$$

Where $a(\mathbf{x})$ denotes the initial condition (and possibly additional input channels encoding parameters). A neural operator \mathcal{G}_θ with trainable parameters θ is trained from pairs $\{a_j, u_j\}_{j=1}^N$, where each a_j is a randomly sampled input function (drawn from a probability distribution μ), and u_j is its corresponding solution, generated by a high-fidelity spectral solver (see [Appendix](#)). Depending on the architecture, \mathcal{G}_θ outputs either the entire time sequence in a single forward pass or predicts one step at a time in an autoregressive manner. In what follows, we briefly review the two baseline architectures and then describe the proposed PENCO framework in detail.

2.2 Four-Dimensional Fourier Neural Operator (FNO-4D)

The FNO [\[37, 51\]](#) learns mappings between function spaces using spectral convolutions. In the classical formulation, a neural operator

$$\mathcal{G}_\theta: \mathcal{A} \rightarrow \mathcal{U} \quad (3)$$

is represented as a composition of a lifting operator, a sequence of spectral layers, and a projection operator. Given an input function $a(\mathbf{x})$, the network first lifts it into a latent representation

$$v_0(\mathbf{x}, t) = \mathcal{P}(a(\mathbf{x}, t)), \quad (4)$$

where \mathcal{P} is a shallow fully connected network acting channel-wise. Each subsequent layer τ performs a combination of local and global operations:

$$v_{\tau+1}(\mathbf{x}, t) := \sigma \left(\mathcal{W}_\tau v_\tau(\mathbf{x}, t) + \mathcal{F}^{-1} \left(R_\tau \circ \mathcal{F}(v_\tau)(\mathbf{k}, t) \right) \right), \quad \forall \mathbf{x} \in \Omega, t \in [0, T] \quad (5)$$

where \mathcal{W}_τ is a pointwise linear map, \mathcal{F} and \mathcal{F}^{-1} denote the forward and inverse spatial Fourier transforms, R_τ is a learnable spectral multiplier defined in the wavenumber domain \mathbf{k} , and σ is a nonlinear activation function. In the FNO-4D variant used here, the Fourier transform acts only on the spatial coordinates $\mathbf{x} = (x, y, z)$, while the wavenumber vector $\mathbf{k} = (k_x, k_y, k_z)$, represents the corresponding spectral modes. Time is treated as an additional input channel rather than a transformed dimension, allowing the model to process multiple time frames in parallel while still leveraging global spatial mixing through spectral convolutions.

This architecture can be expressed compactly as the compositional mapping

$$\mathcal{G}_\theta(a)(\mathbf{x}, t) := \mathcal{Q} \circ \sigma \left[\underbrace{((\mathcal{W}_\tau + \mathcal{K}_\tau) \circ \dots \circ (\mathcal{W}_1 + \mathcal{K}_1))}_{T \text{ iterative layers}} \right] \circ \mathcal{P}(a(\mathbf{x}, t)), \quad (6)$$

where \mathcal{Q} denotes the final projection layer, \mathcal{W}_τ are local linear transformations, and \mathcal{K}_τ represent nonlocal spectral convolutions. Each \mathcal{K}_τ operates by transforming the latent feature map into Fourier space, scaling its spectral coefficients with a learnable complex-valued filter $R_\tau(\mathbf{k})$, and then projecting it back to the spatial domain. This formulation allows the network to learn global interactions through spectral mixing, while \mathcal{W}_τ capture localized spatial dependencies. The trainable parameters θ are optimized to minimize the data mean-squared error

$$\min_{\theta} \frac{1}{N} \sum_{j=1}^N \|\mathcal{G}_\theta(a_j) - u_j\|_2^2, \quad (7)$$

ensuring that the learned operator approximates the true mapping between initial conditions and their corresponding spatiotemporal true solutions u_j .

Unlike autoregressive FNO-3D models, which propagate the solution step by step, FNO-4D takes a block of input time slices and predicts the corresponding block of future states in a single forward pass. This design eliminates hidden-state recurrence and reduces explicit error accumulation, but it does not enforce a causal structure between successive time steps at the architectural level. In this work, FNO-4D serves as a strong data-driven baseline that captures rich spatiotemporal correlations but does not incorporate explicit physical or numerical constraints ([Figure 2-1](#)).

2.3 Multi-Head Neural Operators (MHNO)

The MHNO [50] was proposed to address the complementary limitations of autoregressive error accumulation and non-causal parallel prediction. MHNO retains a spectral neural-operator backbone for spatial processing but introduces a more expressive temporal structure via time-step-specific heads.

First, the initial condition $a(\mathbf{x})$ is passed through a shared spectral encoder (similar in spirit to FNO) to produce a high-dimensional latent representation

$$v_a(\mathbf{x}) := (\mathcal{W}_L + \mathcal{K}_L) \circ \dots \circ (\mathcal{W}_1 + \mathcal{K}_1) \circ \mathcal{P}(a(\mathbf{x})) \quad (8)$$

where \mathcal{W}_L is Fourier integral operators and \mathcal{K}_L is local linear transforms. This encoder is reused for all time steps, providing a shared spatial feature space. At its core, MHNO replaces the static projection operator \mathcal{Q} with a combination of a shared spatial feature extractor and two dynamic, time-step-specific components: projection networks $\{\mathcal{Q}_n\}_{n=1}^{N_t}$ and temporal transition networks $\{\mathcal{H}_n\}_{n=2}^{N_t}$. This dual-component design explicitly couples adjacent time steps, enabling dynamic feature extraction and information passing across the temporal domain. The resulting operator can be written schematically as

$$\mathcal{G}_\theta(a)(\mathbf{x}, t_n) := \begin{cases} \mathcal{Q}_n(v_a(\mathbf{x})), & \text{for } n = 1, \\ \mathcal{Q}_n(v_a(\mathbf{x})) + \mathcal{H}_n(\mathcal{G}_\theta(a)(\mathbf{x}, t_{n-1})), & \text{for } n > 1. \end{cases} \quad (9)$$

This design allows MHNO to predict all time steps in a single forward pass, while maintaining explicit temporal coupling through \mathcal{H}_n . In practice, MHNO improves temporal coherence and stability relative to purely recurrent or fully parallel architectures.

The introduction of time-step-specific projection networks \mathcal{Q}_n and transition operators \mathcal{H}_n gives MHNO a hierarchical interpretation: the shared spectral encoder captures global spatial correlations, while the temporal components act as dynamic filters that adaptively refine features at each time level. This enables the network to represent complex, non-stationary dynamics and long-range temporal dependencies without the need for recurrent hidden states. Each temporal head \mathcal{Q}_n effectively learns the mapping from the encoded spatial field to the corresponding solution snapshot, and the transition networks \mathcal{H}_n propagate information across successive time frames, ensuring causal continuity. Together, these mechanisms allow MHNO to model intricate spatiotemporal behaviors, such as phase evolution, interface migration, and pattern coarsening, within a unified operator-learning framework ([Figure 2-1](#)).

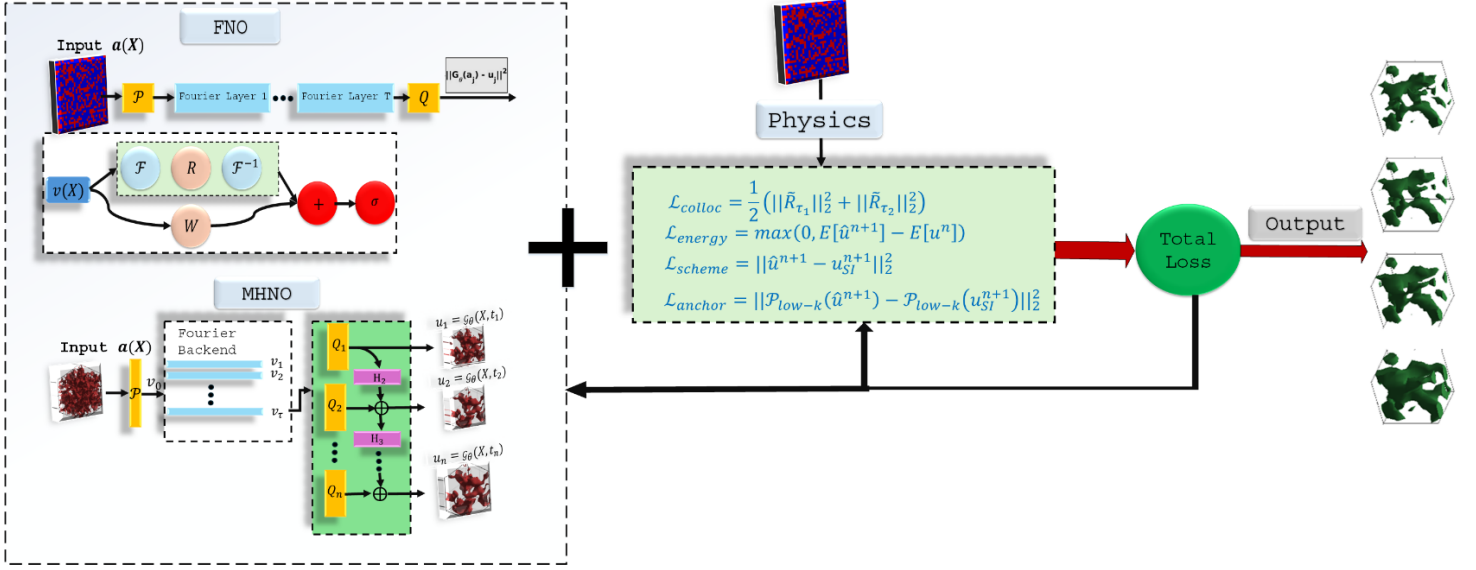


Figure 2-1: Schematic overview of the PENCO framework combining data-driven neural operators (FNO, MHNO) with physics-based losses to form a unified hybrid model ensuring both data accuracy and physical consistency.

2.4 Physics-Guided Loss Design in PENCO

The PENCO framework embeds physical laws, energetic principles, and numerical consistency directly into the learning objective, enabling the model to evolve fields in a manner that remains faithful to both the governing equations and the intrinsic thermodynamic structure of phase-field systems. Rather than treating the loss function as a purely data-driven regression, PENCO formulates it as a structured optimization problem in which each term enforces a distinct aspect of the physical and numerical behavior of the underlying PDE. The overall loss therefore combines data supervision with physics-based constraints, coupling observed trajectories with principles of governing dynamics, energy dissipation, temporal coherence, and spectral stability.

To train the neural operator \mathcal{G}_θ , PENCO combines a standard data-fitting term with a physics-guided regularization term. The total objective is expressed as

$$\mathcal{L}_{total} = (1 - \lambda)\alpha\mathcal{L}_{data} + \lambda\mathcal{L}_{phys}, \quad \lambda = [0,1], \quad (10)$$

where the coefficient α provides a scaling factor that balances the magnitudes of the data and physics terms, ensuring that neither dominates the optimization. In practice, α is chosen such that the two contributions remain of comparable order during training, allowing the model to learn consistently from both empirical trajectories and physical constraints. For all case studies in this work α is set either 10^2 or 10^3 , depending on the characteristic scales of the governing equation, ensuring that the data and physics contributions remain comparable throughout training. The data loss measures direct prediction error against ground truth,

$$\mathcal{L}_{data} = ||\hat{u}^{n+1} - u_{true}^{n+1}||_2^2 \quad (11)$$

and \mathcal{L}_{phys} represents the physics-informed component that constrains the model to obey the governing dynamics.

The physics-based regularization term integrates four complementary components, each addressing a different aspect of physical or numerical fidelity,

$$\mathcal{L}_{phys} = w_1(\mathcal{L}_{colloc} + w_2\mathcal{L}_{anchor}) + w_3\mathcal{L}_{scheme} + w_4\mathcal{L}_{energy} \quad (12)$$

where \mathcal{L}_{colloc} enforces the differential dynamics by evaluating the PDE residual at Gauss–Lobatto points. This penalizes any mismatch between the predicted field and the local PDE behavior, ensuring that the network does not drift into non-physical trajectories even when the data term is weak or noisy.

\mathcal{L}_{scheme} promotes temporal consistency by comparing each predicted update with a stable reference evolution of the PDE. Instead of using a fully explicit step, which would become unstable for stiff phase field models, the reference update applies the linear smoothing operator in Fourier space together with the nonlinear term. This produces a well-conditioned target that reflects the natural interaction of diffusion and nonlinearity and provides a reliable guide for the network during training.

\mathcal{L}_{energy} enforces thermodynamic admissibility by penalizing any increase in the free energy, ensuring that the predicted evolution follows the natural energy-dissipating behavior of phase-field systems and does not produce non-physical growth of energetic modes.

The low-frequency (\mathcal{L}_{anchor}) anchor term penalizes discrepancies between the large-scale Fourier modes of the predicted field and those of the physics-based semi-implicit update. This prevents slow spectral drift or unphysical growth of large-scale structures during training which is a common failure mode of neural operators.

The epoch-dependent weights w_2 and w_3 evolve smoothly during training as

$$w_2(e) = 0.25 + 0.6 \left(\frac{e}{E-1} \right)^2, \quad w_3(e) = 0.32 - 0.12 \frac{e}{E-1} \quad (13)$$

where e denotes the current epoch and E the total number of epochs. In all experiments, we fix $w_1 = 10^{-3}$ for the collocation–anchor block and $w_4 = 0.3$ for the energy term, which keeps their scales consistent with the scheme loss and prevents any component from dominating the optimization. The epoch dependent weights $w_2(e)$ and $w_3(e)$ then adjust the remaining contributions during training. At the beginning of training the scheme consistency term plays a stronger role and helps the model settle into stable short horizon updates. As training progresses, the increasing influence of the anchor term reinforces long range spectral stability and suppresses low frequency drift. This gradual shift in emphasis ensures smooth convergence and maintains a balanced interaction among all physics-based components across the different phase field models.

Together, these components guide the network to capture both the local PDE behavior and the global energetic trends characteristic of phase-field systems, achieving stability, accuracy, and generalization even in data-scarce regimes.

2.4.1 L^2 Gauss–Lobatto Collocation Residual (P)

To ensure that the predicted field evolution satisfies the governing partial differential equation not only at discrete time levels but also within each time step, PENCO employs an L^2 Gauss–Lobatto collocation residual. Let $u(\mathbf{x}, t)$ be a scalar field on a periodic cube $\Omega = [-L/2, L/2]^3$ evolving by a phase-field-type PDE

$$\partial_t u = \mathcal{D}(u), \quad (14)$$

the residual over a time step $[t_n, t_{n+1}]$ with increment Δt is defined as

$$R_\tau = \frac{\hat{u}^{n+1} - u^n}{\Delta t} - \mathcal{D}((1 - \tau)u^n + \tau\hat{u}^{n+1}), \quad (15)$$

where R_τ is the PDE's residual at Gauss–Lobatto collocation points, and $\tau \in [0, 1]$ denotes the normalized collocation location. With a uniform time step Δt , we denote $u^n(\mathbf{x}) \approx u(\mathbf{x}, t_n)$, $t_{n+1} = t_n + \Delta t$, and the neural operator \mathcal{G}_θ predicts the next state $\hat{u}^{n+1} = \mathcal{G}_\theta(u^n)$. PENCO adopts two symmetric Gauss–Lobatto nodes,

$$\tau_{1,2} \in \left\{ \frac{1}{2} \pm \frac{1}{2\sqrt{5}} \right\}, \quad (16)$$

which provide balanced sampling around the temporal midpoint and enhance stability during training. To improve numerical robustness, the residuals are computed in a normalized form,

$$\tilde{R}_\tau = \frac{\dot{u}^n}{\|\dot{u}^n\|_2} - \frac{\mathcal{D}(u_\tau)}{\|\mathcal{D}(u_\tau)\|_2}, \quad (17)$$

where $\dot{u}^n = (\hat{u}^{n+1} - u^n)/\Delta t$ and $u_\tau = (1 - \tau)u^n + \tau\hat{u}^{n+1}$. This normalization stabilizes gradient magnitudes during early training and balances the relative influence of stiff linear and nonlinear components, leading to smoother convergence. The associated loss term is then expressed as $\mathcal{L}_{\text{colloc}}$

$$\mathcal{L}_{\text{colloc}} = \frac{1}{2} (\|\tilde{R}_{\tau_1}\|_2^2 + \|\tilde{R}_{\tau_2}\|_2^2), \quad (18)$$

This symmetric two-point evaluation strongly enforces temporal consistency, balances the magnitudes of temporal and spatial errors, and serves as the dominant accuracy-enhancing mechanism within the PENCO formulation.

2.4.2 Energy consistency (E)

Most phase-field models arise as gradient flows of a free-energy functional, and their physical solutions satisfy a monotonic decay of the total free energy over time. If $E[u]$ denotes the free energy of the state $u(\mathbf{x}, t)$, then the thermodynamic structure of these models requires $E[u^{n+1}] \leq E[u^n]$ at every discrete time step, ensuring that the system relaxes toward equilibrium rather than accumulating artificial energy. In general, the free energy consists of a bulk contribution together with gradient-dependent regularization terms. A common representation is

$$E[u] = \int_{\Omega} \left(F(u) + \frac{1}{2} \epsilon^2 |\nabla u|^2 + H(u, \nabla u, \Delta u, \dots) \right) d\mathbf{x}, \quad (19)$$

where $F(u)$ denotes the local thermodynamic potential (often a double-well form), the gradient term $\frac{1}{2} \epsilon^2 |\nabla u|^2$ penalizes sharp interfaces and introduces the characteristic interface width ϵ , and the functional $H(\cdot)$ accounts for higher-order spatial derivatives that appear in extended phase-field models such as PFC and MBE.

A conventional numerical discretization enforces this energetic decay by construction, but a purely data-driven neural operator may violate it, producing spurious increases in energy and unstable long-horizon rollouts. To prevent such behavior, PENCO introduces a one-sided dissipation penalty,

$$\mathcal{L}_{energy} = \max(0, E[\hat{u}^{n+1}] - E[u^n]), \quad (20)$$

which activates only if the predicted update increases the free energy. This guarantees that the learned dynamics remain consistent with the variational structure of the PDE, improving long-term stability and regularizing the solution at a global thermodynamic level, complementary to the local PDE residual and scheme consistency constraints.

2.4.3 Numerical (scheme) Consistency (N)

In addition to enforcing PDE residuals directly, PENCO further improves stability by aligning the network's predictions with a semi-implicit time-stepping scheme that is widely used in numerical simulations of phase-field models. Such schemes are based on the implicit–explicit (IMEX) principle, where stiff linear terms $L(u)$ are treated implicitly to enhance stability, while nonlinear terms $\mathcal{N}(u)$ are evaluated explicitly to avoid solving nonlinear systems at each step. Let the general phase-field PDE be written in operator-split form as

$$\frac{u^{n+1} - u^n}{\Delta t} = -\mathcal{M}(L(u^{n+1}) + \mathcal{N}(u^n)), \quad (21)$$

where \mathcal{M} is the mobility operator that defines the geometry of the gradient flow (for instance, $\mathcal{M} = I$ in AC, and $\mathcal{M} = -\Delta$ in CH). The above relation can be rearranged into the linear system

$$(I + \Delta t \mathcal{M}L)u^{n+1} = u^n - \Delta t \mathcal{M}\mathcal{N}(u^n), \quad (22)$$

solving this expression yields the semi-implicit (SI) numerical update

$$u_{SI}^{n+1} = (I + \Delta t \mathcal{M}L)^{-1}(u^n - \Delta t \mathcal{M}\mathcal{N}(u^n)), \quad (23)$$

which we refer to as the numerical teacher. This u_{SI}^{n+1} is not a learned quantity but the deterministic update produced by the IMEX scheme when starting from state u^n . To encourage the neural operator to remain consistent with this stable evolution, PENCO introduces the scheme consistency loss

$$\mathcal{L}_{scheme} = ||\hat{u}^{n+1} - u_{SI}^{n+1}||_2^2, \quad (24)$$

which penalizes deviations from the IMEX update. This consistency term serves a dual purpose. First, by aligning the model predictions with a semi-implicit IMEX update, it transfers the inherent stability of numerical solvers into the learning process and prevents the uncontrolled accumulation of errors over long horizons. Second, it guides the neural operator to respect the natural linear–nonlinear splitting structure of the governing PDE, which enhances its ability to generalize beyond the specific training data.

To further reinforce stability at large spatial scales, the scheme consistency is extended into the spectral domain through a low-frequency anchoring constraint, which minimizes deviations between the coarse Fourier components of the prediction and those of the semi-implicit reference:

$$\mathcal{L}_{anchor} = ||\mathcal{P}_{low-k}(\hat{u}^{n+1}) - \mathcal{P}_{low-k}(u_{SI}^{n+1})||_2^2, \quad (25)$$

where $\mathcal{P}_{low-k}(\cdot)$ denotes projection onto the lowest-wavenumber fraction of the spectrum. This spectral anchoring prevents phase drift and unphysical growth of long-wavelength modes, thereby preserving coherent large-scale structures throughout training. Together, the real-space and spectral components of numerical consistency provide PENCO with strong stability and accuracy across extended temporal horizons.

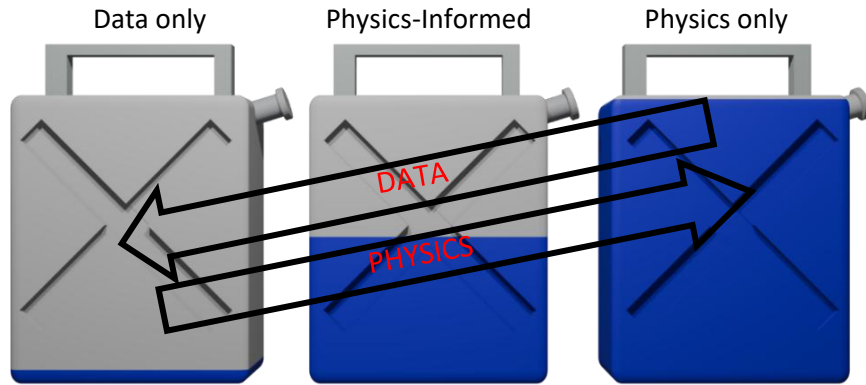


Figure 2-2: A conceptual illustration of training paradigms. PENCO employs the hybrid strategy (center), where the model is filled with knowledge from both data and physics to ensure physical consistency.

3 Data Generation and Training–Budget Protocol

3.1 Data – Generation

Unlike purely data-driven neural operators, which heavily depend on large simulation corpora to achieve acceptable accuracy, PENCO is designed to operate effectively even when only a very limited number of trajectories are available. In our experiments, the training regime intentionally reflects this data-scarce setting, with only $N = \{50, 100, 200\}$ trajectories provided for supervision. These datasets serve merely as auxiliary physical examples, while the governing dynamics are primarily learned through the physics-based loss components.

The reference trajectories are obtained by numerically integrating five benchmark three-dimensional phase-field models (AC, CH, SH, PFC, and MBE) on periodic cubic domains. The simulations are carried out using a Fourier-spectral discretization [7] in space combined with a semi-implicit time integrator, a formulation that provides high numerical fidelity and excellent stability for long-horizon phase-field dynamics. The detailed mathematical formulation and implementation of this spectral solver are provided in [Appendix A](#). Each trajectory is initialized from a randomized Gaussian Random Field whose statistical parameters are resampled for every simulation, producing a diverse ensemble of physically plausible morphologies without requiring any handcrafted or engineered initial seeds. This stochastic initialization mechanism naturally spans a wide distribution of interface geometries, characteristic wavelengths, and phase-separation patterns, thereby supplying minimal but sufficiently rich supervision to guide the operator during training.

A key objective in our data generation strategy was to create a rich and diverse set of initial conditions to ensure our trained models are robust and can generalize effectively. To achieve this, we employed a two-pronged approach. The primary method involved initializing simulations with Gaussian Random Fields (GRFs). Crucially, rather than using fixed statistical parameters, we randomized the GRF's controlling parameters and the subsequent thresholding value for each simulation. This process generated a wide spectrum of initial random morphologies with varying characteristic length scales and volume fractions.

All numerical generation and training are executed within an environment based on PyTorch, using NVIDIA A100 GPU. This ensures that the same floating-point conventions are preserved between numerical ground truth and neural operator training, avoiding solver–model mismatch.

3.2 Training–Budget Protocol

A central goal of this study is to assess neural operator performance in a data-scarce regime, where only a limited number of reference trajectories are available for supervision. Accordingly, we consider training sets of size $N = \{50, 100, 200\}$, which are one to two orders of magnitude smaller than those typically required by purely data-driven neural operators (which often rely on $\sim 2000 - 5000$ trajectories to achieve stable accuracy). To enable a fair comparison across different dataset sizes and across learning regimes (data-driven, hybrid, and pure-physics), we enforce two safeguards:

3.2.1 Fixed evaluation set

The held-out test set consists of a constant number of trajectories (50 for every PDE), ensuring that evaluation is stable and directly comparable across dataset sizes.

3.2.2 Fixed optimization budget

The number of gradient updates is kept constant for a given PDE, independent of the number of available training trajectories. This prevents larger datasets from implicitly receiving more optimizer steps and therefore more learning opportunity. In the pure-physics limit ($\lambda = 1$), this guarantee is essential: the model should improve because it better satisfies the PDE, not because it was allowed to take more gradient steps.

A consistent neural architecture is maintained throughout all experiments, employing a compact spectral operator with two layers, moderate latent width, and approximately 800k trainable parameters. The design is balanced for expressivity and stability in 3D spatiotemporal learning on 32^3 grids. [Table 3-1](#) summarizes our fixed-budget training protocol, where the base steps per epoch (SPE) were determined empirically to balance accuracy against computational requirements. Effective SPE scales with dataset size relative to the reference ($N_{ref} = 50$) as $SPE \times (N/N_{ref})$. Total gradient updates (the count of optimizer weight updates) are computed as effective $SPE_{eff} \times Epoch$ for hybrid training ($\lambda \neq 1$), while pure physics ($\lambda = 1$) uses the fixed base $SPE \times Epoch$ to maintain constant computational budget regardless of dataset size. This computational budgeting strategy ensures that performance differences across $N = 50, 100, 200$ arise solely from data efficiency rather than hidden computational advantages. Finally, the average epoch time in the last column reflects PENCO training under the MHNO architecture with a hybrid weighting set to $\lambda = 0.25$.

Table 3-1: Training protocol and computational budget across phase-field equations.

PDEs	N	Batch	SPE	Epoch	SPE_{eff} $\lambda \neq 1$	Total updates $\lambda = 1$	Total updates $\lambda \neq 1$	Avg. epoch time (s)
AC	50	8	10	50	10	500	500	0.27
	100	8	10	50	20	500	1000	0.63
	200	8	10	50	40	500	2000	1.15
CH	50	8	30	50	30	4000	1500	2.1
	100	8	30	50	60	4000	3000	3.9
	200	8	30	50	120	4000	6000	8.1
SH	50	8	5	150	5	750	750	0.42
	100	8	5	150	10	750	1500	0.86
	200	8	5	150	20	750	3000	1.45
PFC	50	8	10	50	10	500	500	0.79
	100	8	10	50	20	500	1000	1.7
	200	8	10	50	40	500	2000	3.3
MBE	50	8	30	50	30	1500	1500	3.71
	100	8	30	50	60	1500	3000	6.71
	200	8	30	50	120	1500	6000	12.13

4 Numerical Experiments

This section evaluates the performance of the proposed physics-guided neural operator PENCO in comparison with the data-driven frameworks FNO-4D and MHNO across five standard three-dimensional phase-field equations. These benchmarks collectively capture interfacial motion, phase separation, and pattern-forming dynamics, and are unified under the generalized formulation

$$\begin{aligned} \frac{\partial u}{\partial t} = & \alpha_1 \left[\nabla^2 u - \frac{1}{\epsilon^2} f'(u) \right] + \alpha_2 \nabla^2 [-\epsilon^2 \nabla^2 u + f'(u)] + \alpha_3 [-u^3 - (1 - \epsilon)u + 2\nabla^2 u - \nabla^4 u] \\ & + \alpha_4 \nabla^2 [u^3 + (1 - \epsilon)u + 2\nabla^2 u + \nabla^4 u] + \alpha_5 [-\epsilon \nabla^4 u - \nabla \cdot ((1 - |\nabla u|^2) \nabla u)] \\ u(x, 0) = & u_0(x), \quad x \in [-L/2, L/2], \quad t \in (0, T] \end{aligned} \quad (26)$$

where u_0 denotes the prescribed initial field. The spatial domain is periodic and defined over x , with time t . The coefficients $\alpha_1, \dots, \alpha_5$ specify the governing models, AC, CH, SH, PFC, and MBE respectively.

Each equation is simulated using four surrogate models, FNO-4D, MHNO, the proposed hybrid PENCO, and a pure-physics operator, and all predictions are directly compared against high-fidelity numerical reference solutions generated by a semi-implicit Fourier-spectral solver. All models are trained under identical data-scarce regimes and evaluated using the same spatial resolution and time-stepping parameters.

To assess predictive accuracy, all neural operators are evaluated against the high-fidelity numerical solution using the normalized L_2 -error

$$\text{Error} = \frac{\sqrt{\sum_{i=1}^N |\mathcal{U}(x_i, t_i) - u(x_i, t_i)|^2}}{\sqrt{\sum_{i=1}^N |u(x_i, t_i)|^2}}, \quad (27)$$

where $u(x_i, t_i)$ denotes the reference field and $\mathcal{U}(x_i, t_i)$ the model prediction at discrete space–time samples. This metric provides a uniform measure of deviation from the true dynamics and enables consistent quantitative comparison across all PDEs, resolutions, and rollout lengths.

4.1 In-Distribution Performance

4.1.1 Phase Separation Kinetics: The Allen-Cahn Equation

We first benchmark our proposed models on the 3D AC equation, a fundamental model for phase separation and coarsening dynamics. Its versatility makes it a cornerstone in computational science, with its explicit use in wide-ranging applications such as simulating ductile fracture [52], interface dynamics simulation [53], and crystal growth [54]. Within our unified phase-field formulation (Eq. 25), it corresponds to setting $\alpha_1 = 1$ ($\alpha_{2-5} = 0$), yielding

$$\begin{aligned} \frac{\partial u(x, t)}{\partial t} = & \nabla^2 u(x, t) - \frac{1}{\epsilon^2} f'(u(x, t)), \\ u(x, 0) = & u_0(x), \quad x \in [-L/2, L/2], \quad t \in (0, T]. \end{aligned} \quad (28)$$

The system's evolution is governed by the interplay between two terms. The first is the reaction term, derived from the derivative of a double-well energy potential, $f(u) = \frac{1}{4}(u^2 - 1)^2$. Its form, $f'(u) = u^3 - u$, drives the phase field variable u towards one of the two stable, pure-phase states ($u = \pm 1$). This is counteracted by the diffusion term, $\nabla^2 u$, which acts to minimize the interfacial energy between phases, analogous to surface tension, thereby smoothing complex geometries over time. The equation as a whole, $\partial u / \partial t$, describes how these two competing forces evolve the system, with the parameter ϵ balancing them and controlling the thickness of the final interface.

The primary objective is to train a neural operator, \mathcal{G}_θ , that learns the solution operator mapping an initial condition $u_0(\mathbf{x})$ to the full spatiotemporal evolution of the system:

$$\mathcal{G}_\theta: u(\mathbf{x}, 0) \rightarrow \{u(\mathbf{x}, t)\}_{t \in [0, T]} \quad (29)$$

Each trajectory is defined on a uniform grid of 32^3 points, the interface width parameter $\epsilon = 0.1$, and the temporal resolution of $N_t = 100$ with uniform time step-size $\Delta t = 0.0001$.

We first assess the model's performance on test data drawn from the same GRF-based distribution used for training. [Figure 4-1](#) and [Figure 4-2](#) visualize the temporal evolution predicted by FNO-4D, MHNO, and PENCO at $t = \{0, 20, 40, 60, 80, 100\}\Delta t$, compared against the numerical reference. For brevity, the hybrid physics-guided model based on the MHNO architecture is referred to simply as PENCO throughout the plots. [Figure 4-1](#) shows two-dimensional contour slices of the evolving phase boundaries, while [Figure 4-2](#) presents the corresponding three-dimensional iso-surface morphologies that depict the spatial coarsening process in full detail.

Both data-driven baselines reproduce the early-time evolution but gradually drift away from the true dynamics. Their interfaces become overly smooth, small features vanish prematurely, and the connectivity of the phase domains degrades with time. This behavior is most pronounced in FNO-4D, which noticeably diverges from the reference during the later stages of coarsening.

PENCO, trained with a moderate physics weight ($\lambda = 0.25$), retains the correct interfacial geometry and coarsening rate throughout the rollout. It preserves sharp boundaries, maintains domain topology, and remains visually aligned with the reference even at the final time. The physics-guided constraints effectively suppress long-horizon drift, which is a persistent failure mode in purely data-driven operators. The pure-physics configuration ($\lambda = 1.0$) also captures the coarse morphology reliably, confirming the stabilizing role of the PDE structure, although it lacks the finer detail recovered by the hybrid model.

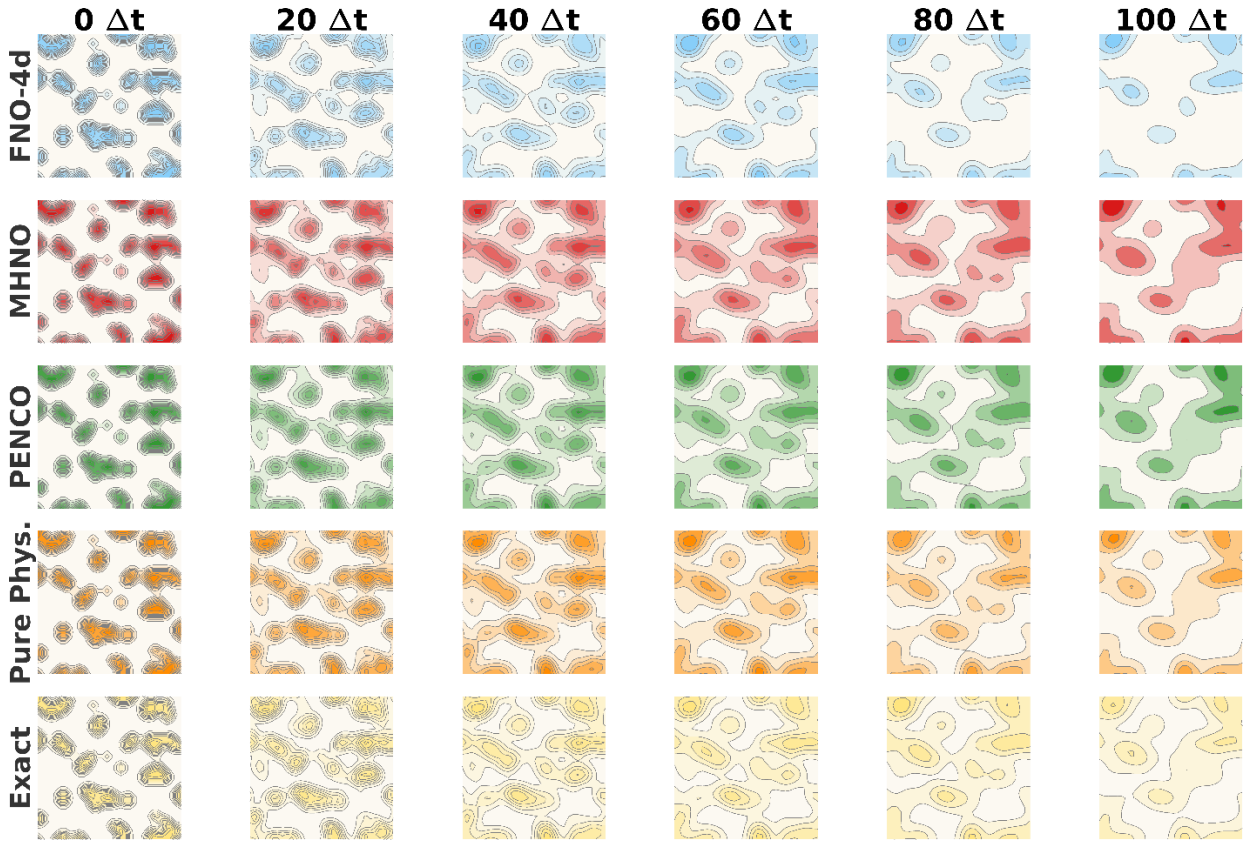


Figure 4-1: Two-dimensional contour evolution of the AC system at selected time steps for FNO-4D, MHNO, PENCO ($\lambda = 0.25$) the pure-physics model, and the numerical reference (32^3 grid, $\Delta t = 0.0001$, $\epsilon = 0.1$, $L = 2$, $N = 100$).

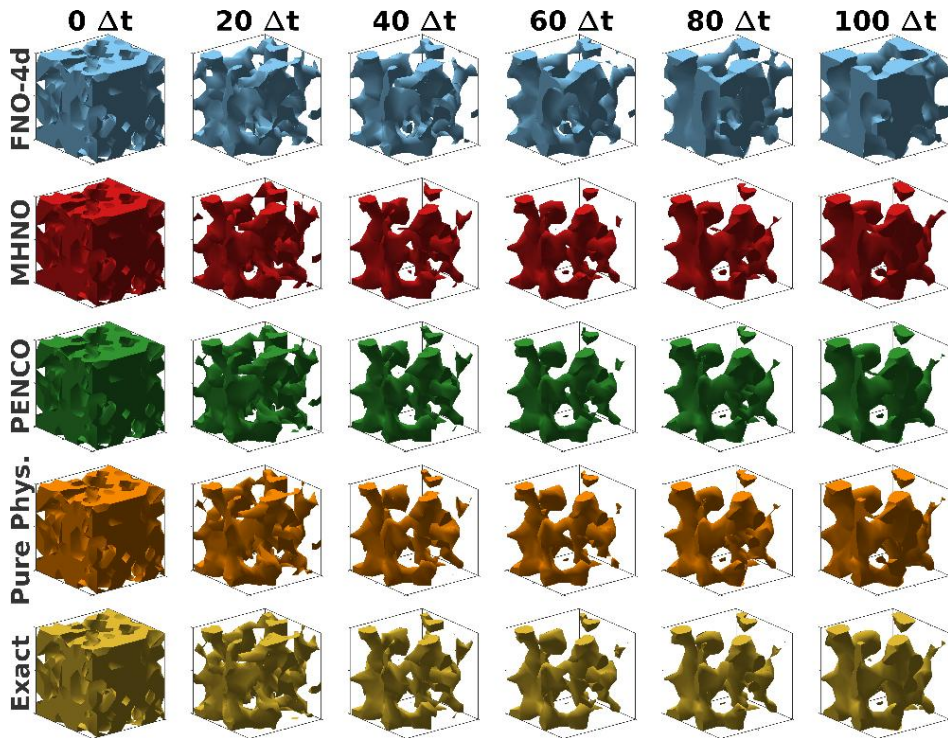


Figure 4-2: Three-dimensional iso-surface evolution of the AC phase field for the same models and simulation parameters as in Figure 4.1.

[Figure 4-3](#) summarizes the convergence behavior and long-horizon accuracy for the AC system using $N = 200$ training samples. The total loss curves clearly distinguish the behavior of the different methods. PENCO converges rapidly and avoids the oscillations observed in the purely data-driven baselines, demonstrating that the physics-guided terms stabilize the optimization process and suppress gradient drift. The pure physics model also converges smoothly, but at a slower rate due to the absence of data supervision.

The relative L_2 error curves highlight the effect of physical regularization during rollout. FNO-4D and MHNO exhibit a pronounced error increase immediately after the initial transient, reflecting the tendency of purely data-driven operators to overshoot when the trajectory leaves the training manifold. In contrast, PENCO maintains a low and nearly time-independent error across the full horizon. Both PENCO variants provide substantially lower error than the baselines, with PENCO-MHNO achieving the best overall stability and accuracy.

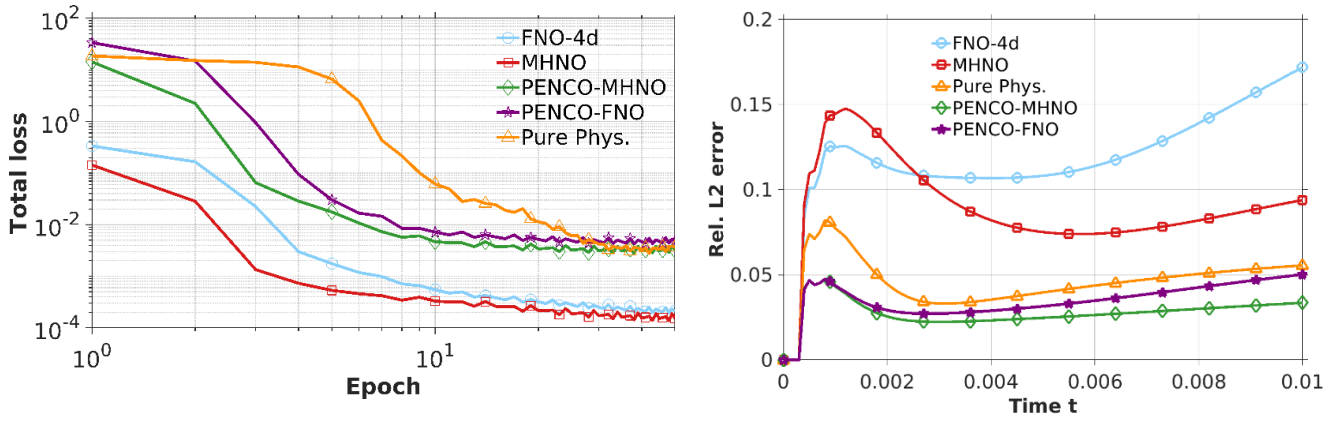


Figure 4-3: Total training loss and relative L_2 -error for the AC system.

The quantitative comparisons in [Table 4-1](#) show that physics-guided regularization produces a substantial reduction in long-horizon error across all data regimes. In the low-data setting with $N = 50$, the PENCO models (built on the MHNO architecture, as in all following tables) achieve a dramatic gain in accuracy, lowering the final-time error by approximately **80–85%** relative to the data-driven baselines. This corresponds to a five- to six-fold improvement, highlighting the critical role of physical structure when training data are scarce. The pure-physics configuration also performs markedly better than both FNO-4D and MHNO, indicating that the PDE constraints alone already stabilize the dynamics and yield reliable predictions.

As the training set increases to $N = 100$, the advantage of the hybrid formulation remains significant. PENCO delivers an accuracy improvement of roughly **70–80%** compared to the baselines, showing that the integration of physics continues to provide superior long-term fidelity even when more data are available. With $N = 200$, the hybrid operators retain a strong margin, improving accuracy by **about 65–70%** relative to MHNO and nearly **90%** relative to FNO-4D. These consistent gains across all training

regimes demonstrate that incorporating the governing physical structure into the learning process substantially enhances both accuracy and stability.

Table 4-1: Relative L_2 norm errors of AC equation ($L = 2$, grid 32^3 , $\epsilon = 0.1$, $\Delta t = 0.0001$).

N	Method	$0\Delta t$	$20\Delta t$	$40\Delta t$	$60\Delta t$	$80\Delta t$	$100\Delta t$
50	FNO-4d	0	0.25	0.24	0.28	0.33	0.37
50	MHNO	0	0.18	0.18	0.24	0.31	0.36
50	PENCO ($\lambda = 0.25$)	0	0.04	0.05	0.06	0.07	0.08
50	PENCO ($\lambda = 0.50$)	0	0.05	0.05	0.06	0.07	0.08
50	PENCO ($\lambda = 0.75$)	0	0.06	0.05	0.06	0.07	0.08
50	Pure Phys. ($\lambda = 1.0$)	0	0.06	0.04	0.05	0.06	0.06
100	FNO-4d	0	0.14	0.12	0.13	0.16	0.2
100	MHNO	0	0.17	0.1	0.08	0.09	0.11
100	PENCO ($\lambda = 0.25$)	0	0.03	0.03	0.03	0.04	0.04
100	PENCO ($\lambda = 0.50$)	0	0.03	0.03	0.03	0.03	0.04
100	PENCO ($\lambda = 0.75$)	0	0.04	0.02	0.03	0.03	0.03
100	Pure Phys. ($\lambda = 1.0$)	0	0.06	0.04	0.05	0.06	0.06
200	FNO-4d	0	0.11	0.11	0.11	0.12	0.16
200	MHNO	0	0.11	0.06	0.06	0.06	0.06
200	PENCO ($\lambda = 0.25$)	0	0.03	0.02	0.02	0.02	0.02
200	PENCO ($\lambda = 0.50$)	0	0.03	0.02	0.02	0.02	0.02
200	PENCO ($\lambda = 0.75$)	0	0.04	0.01	0.01	0.02	0.02
200	Pure Phys. ($\lambda = 1.0$)	0	0.06	0.04	0.05	0.06	0.06

4.1.2 Conserved Phase Separation: The Cahn-Hilliard Equation

The CH equation models conserved phase separation and introduces a higher level of complexity due to its fourth-order spatial operator. Within the unified framework it is obtained by activating the α_2 term, and its dynamics are driven by the Laplacian of the chemical potential, which enforces strict mass conservation and curvature-controlled coarsening. This mechanism underlies a wide range of physical processes, including microstructure evolution in alloys and battery electrodes [55], moving contact lines in confined flows [56], air–water interface dynamics [57], and diffuse-interface tumor growth [58]. The conservation law makes the equation a demanding benchmark for surrogate models, especially when training data are limited.

The CH visualizations in [Figure 4-4](#) and [Figure 4-5](#) show that the three baseline models, FNO-4d, MHNO and the pure physics variant, all gradually lose agreement with the reference solution as time advances. Their predictions increasingly smooth out the interfaces, small domains disappear, and the phase regions begin to lose the correct volume distribution. This behaviour is reflected again in [Figure 4-6](#), where the relative L_2 -error of these three models follows a very similar increasing trend, with the pure physics model only marginally more accurate than the two data based networks. In all three cases the lack of a strong corrective mechanism allows numerical diffusion and small mass imbalance to accumulate and degrade the morphology.

In contrast, PENCO with $\lambda = 0.25$, built on the MHNO architecture, tracks the reference evolution much more faithfully. In [Figure 4-4](#) and [Figure 4-5](#) its contours and iso-surfaces remain close to the numerical solution throughout the rollout, with sharper interfaces, well preserved domain topology and a coarsening rate that matches the ground truth. The corresponding curve in [Figure 4-6](#) stays well below all other methods and shows only mild growth over time. This marked improvement confirms that the added physics guidance is essential for stabilising the conservative dynamics and preventing the long-horizon drift observed in the baseline models.

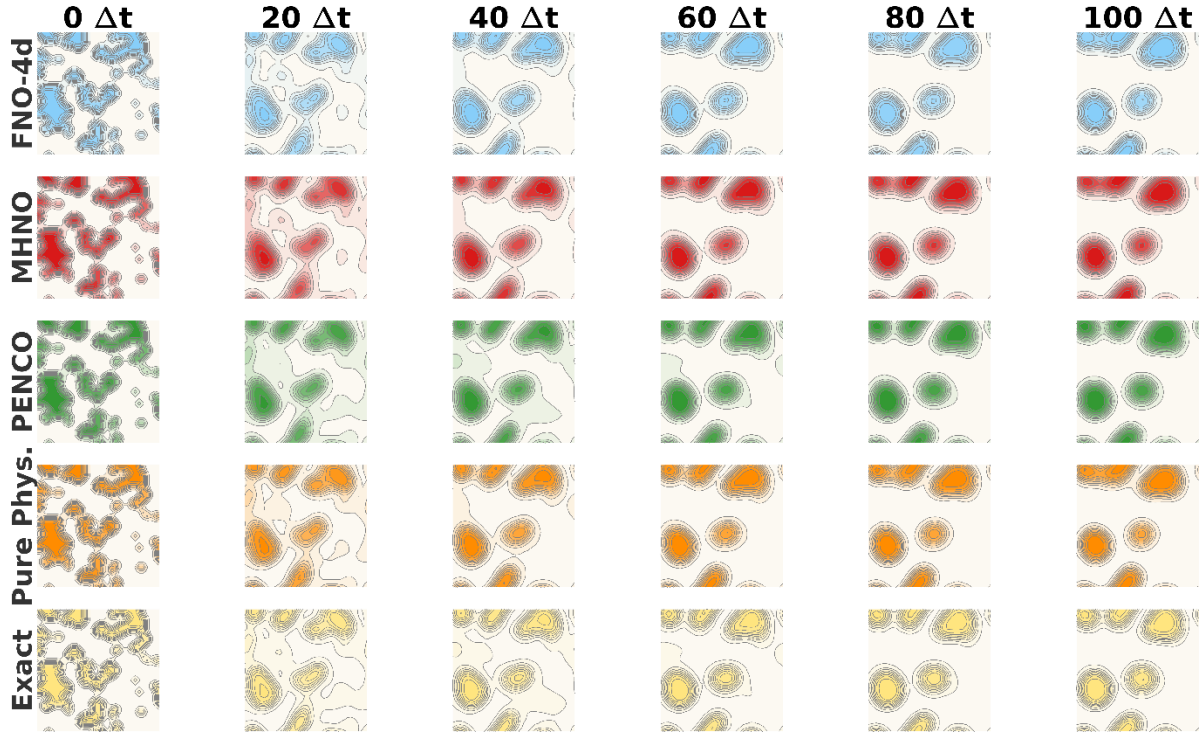


Figure 4-4: 2D contour evolution of the Cahn–Hilliard system for FNO-4d, MHNO, PENCO, the pure-physics model and the reference ($L = 2$, grid 32^3 , $\Delta t = 0.005$, $\epsilon = 0.05$, $N = 200$).

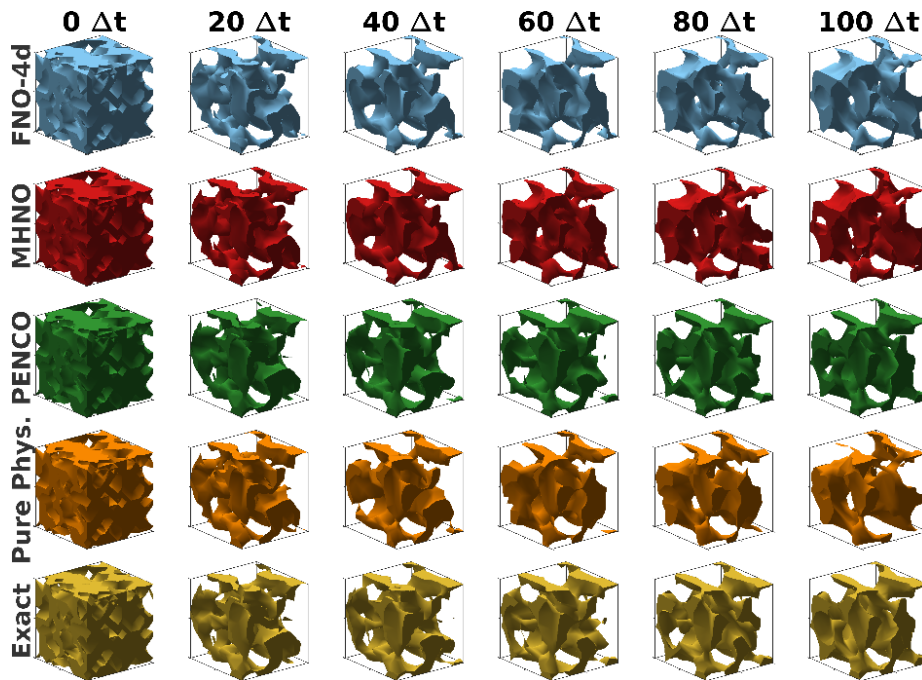


Figure 4-5: 3D iso-surface evolution of the Cahn–Hilliard morphology for the same configurations.

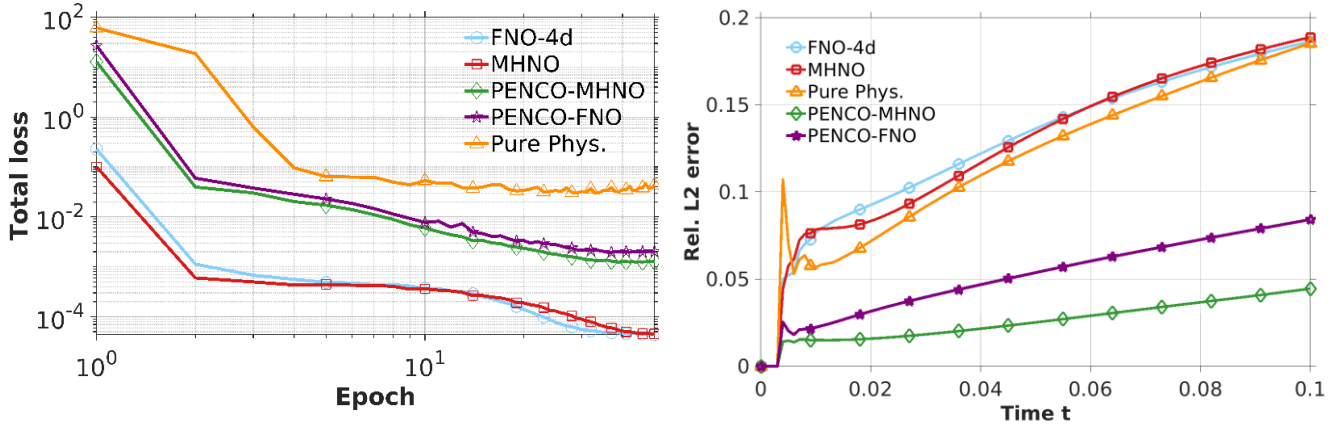


Figure 4-6: Total training loss and relative L_2 -error for the CH system, showing the improved long-horizon accuracy of PENCO compared with all baseline models.

The numerical comparisons in [Table 4-2](#) highlight how strongly the conservation constraint influences predictive accuracy. When the training set is very small ($N = 50$), the three baseline models behave similarly and accumulate error at a comparable rate. The absence of a corrective physical mechanism allows mass imbalance and numerical diffusion to grow, which limits the achievable accuracy even when the architecture is expressive. Introducing physics regularization changes this behaviour immediately. PENCO reduces the long-horizon error by roughly **30–40 percent** compared with the baselines, revealing a clear gain in data efficiency even under the most restrictive conditions.

Increasing the training set to $N = 100$ further exposes the separation between the methods. While FNO-4d and MHNO show only modest benefit from additional data, PENCO achieves errors that are **about 60 percent smaller** across the rollout. The hybrid model is the only configuration that translates the extra data into meaningful long-horizon improvement, demonstrating that accurate CH dynamics require both data and structural guidance.

With $N = 200$, the contrast becomes even more apparent. The baseline methods plateau at nearly the same error levels as in the $N = 100$ case, indicating limited data scalability for this conservative system. In comparison, PENCO reduces the error by **a factor of four to five**, showing that the physics term enables the network to extract and generalize information from the data far more effectively. The pure-physics model remains stable but lacks the refinement gained from data, placing it between the baselines and PENCO.

Table 4-2: Relative L_2 norm errors for CH equation ($L = 2$, grid 32^3 , $\Delta t = 0.005$, $\epsilon = 0.05$)

N	Method	$0\Delta t$	$20\Delta t$	$40\Delta t$	$60\Delta t$	$80\Delta t$	$100\Delta t$
50	FNO-4d	0	0.11	0.16	0.19	0.21	0.23
50	MHNO	0	0.19	0.16	0.17	0.19	0.21

50	PENCO ($\lambda = 0.25$)	0	0.08	0.11	0.14	0.16	0.19
50	PENCO ($\lambda = 0.50$)	0	0.08	0.11	0.14	0.17	0.19
50	PENCO ($\lambda = 0.75$)	0	0.08	0.11	0.14	0.16	0.18
50	Pure Phys. ($\lambda = 1.0$)	0	0.07	0.11	0.14	0.16	0.19
100	FNO-4d	0	0.12	0.15	0.18	0.19	0.2
100	MHNO	0	0.1	0.13	0.16	0.18	0.2
100	PENCO ($\lambda = 0.25$)	0	0.03	0.04	0.06	0.08	0.09
100	PENCO ($\lambda = 0.50$)	0	0.03	0.05	0.06	0.08	0.09
100	PENCO ($\lambda = 0.75$)	0	0.03	0.05	0.06	0.08	0.09
100	Pure Phys. ($\lambda = 1.0$)	0	0.07	0.11	0.14	0.16	0.19
200	FNO-4d	0	0.09	0.12	0.15	0.17	0.19
200	MHNO	0	0.08	0.12	0.15	0.17	0.19
200	PENCO ($\lambda = 0.25$)	0	0.02	0.02	0.03	0.04	0.04
200	PENCO ($\lambda = 0.50$)	0	0.02	0.02	0.03	0.04	0.04
200	PENCO ($\lambda = 0.75$)	0	0.02	0.02	0.03	0.04	0.05
200	Pure Phys. ($\lambda = 1.0$)	0	0.07	0.11	0.14	0.16	0.19

4.1.3 Spontaneous Pattern Formation: The Swift-Hohenberg Equation

The SH equation governs spontaneous pattern formation in systems where periodic structures emerge from initially uniform states. It plays a central role in the formation of convection rolls in heated fluids [59] and in characterizing wrinkle formation in thin elastic films [60]. In the unified framework this model is obtained by activating the α_3 term, producing a dynamics governed by the interaction between a growth-inducing Laplacian and a stabilizing biharmonic operator. Their competition selects a preferred spatial frequency, leading to the striped or cellular morphologies characteristic of SH evolution.

The SH dynamics provide a stringent test for surrogate models because the preferred wavelength and phase of the stripes must remain coherent over long times. The visual comparisons in [Figure 4-7](#) and [Figure 4-8](#) illustrate how sensitive the system is to small phase or curvature deviations. Patterns predicted by the data-driven baselines gradually drift as the evolution proceeds. Their stripes become slightly displaced, locally smoothed, or misaligned near defect regions. This behaviour is most pronounced for FNO-4D, which departs from the reference pattern earliest and with the largest shift. MHNO retains structure longer but ultimately exhibits the same trend, since neither method incorporates the wavelength selection that governs SH morphology.

The hybrid PENCO models ($\lambda = 0.25$) maintain the spacing, phase, and overall coherence of the striped patterns with far higher fidelity. By combining PDE-based stabilization with data-driven correction, the model keeps the emergent wavelength locked while accurately resolving nonlinear interactions that pure physics cannot capture. The PENCO variant built on MHNO achieves the most consistent alignment with the reference across all time frames and preserves the fine-scale oscillatory features of the pattern.

The purely physics-based configuration behaves differently in this system compared with others. After the first second of evolution its accuracy drops below that of the MHNO baseline. This decline is explained by the sensitivity of the SH equation to small phase and amplitude discrepancies. The PDE alone maintains global structure but cannot correct the fine nonlinear adjustments required to keep the stripes perfectly

aligned. Without data supervision, small errors in curvature and phase accumulate until the predicted pattern slowly shifts away from the true solution.

[Figure 4-9](#) shows that both data driven models and the pure physics solver exhibit an initial error overshoot. The data driven methods lack the wavelength selection mechanism of the SH equation, while the pure physics model lacks data supervision during the rapid growth phase. After this transient, FNO 4d and MHNO accumulate phase drift and their errors steadily increase, whereas the PENCO variants remain stable with consistently low errors. The pure physics model, although less accurate than MHNO for most of the rollout, gradually closes the gap and approaches the MHNO accuracy by the final time frame.

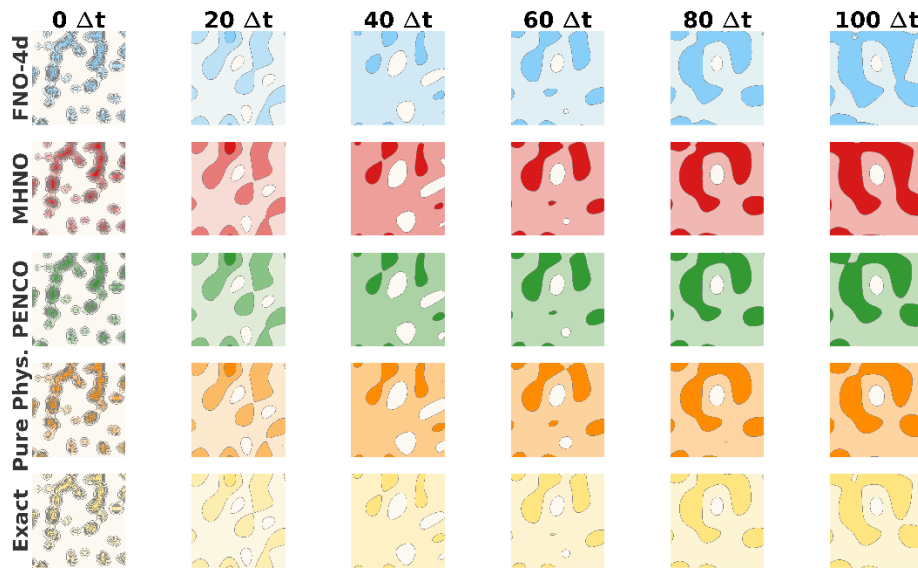


Figure 4-7: Two-dimensional contour evolution for the SH system comparing FNO-4d, MHNO, PENCO, pure-physics, and the reference solution ($L = 15$, grid 32^3 , $\Delta t = 0.05$, $\epsilon = 0.15$, $N = 200$).

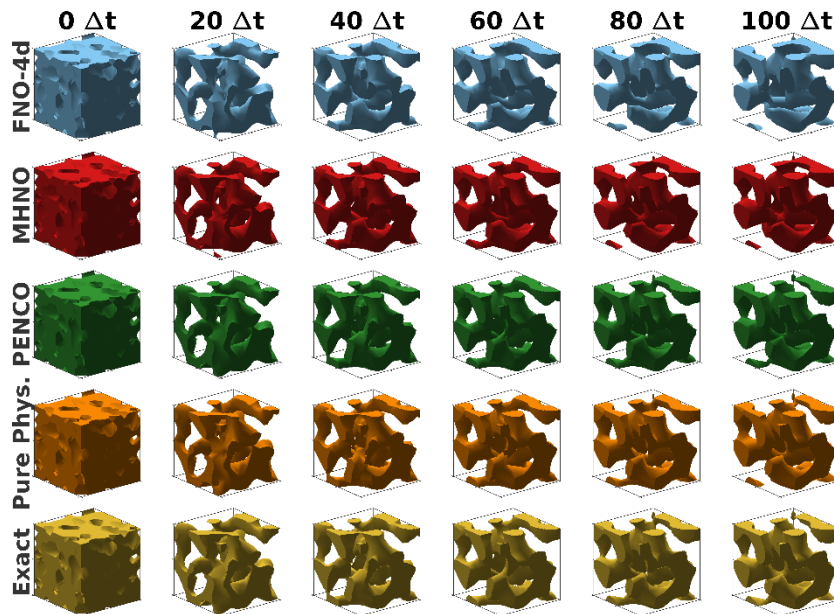


Figure 4-8: Three-dimensional iso-surface visualization of SH pattern formation across all methods.

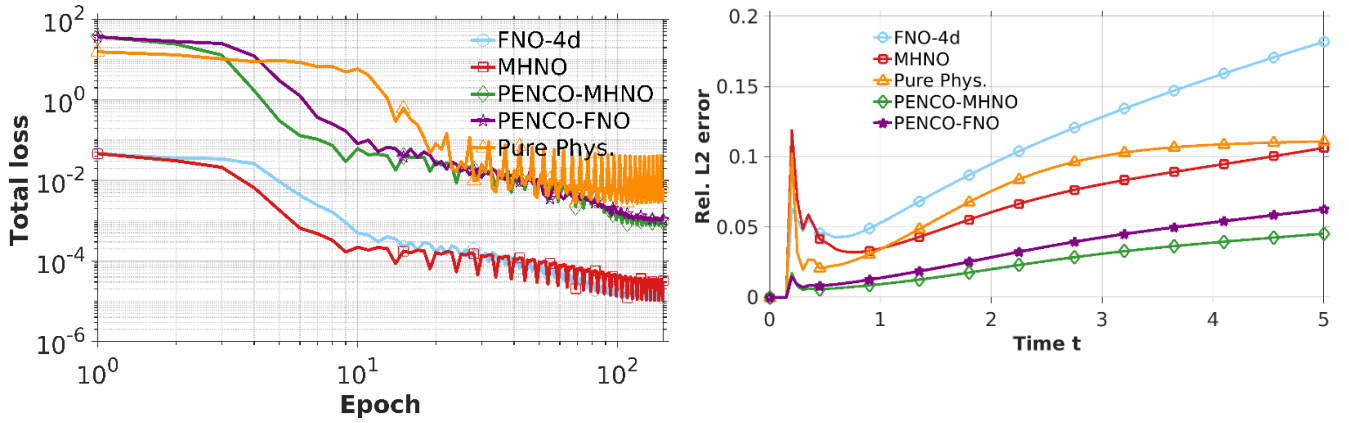


Figure 4-9: Total loss and relative L_2 -error for the SH system showing stable long-horizon accuracy of the PENCO models and overshoot followed by drift in the data-driven baselines.

The quantitative results in [Table 4-3](#) show that adding physics information produces a clear and systematic improvement across all dataset sizes. For $N = 50$, the data-driven baselines settle at relatively large final errors, whereas the PENCO variants reduce the discrepancy by a factor of about two to three. This corresponds to an accuracy gain from roughly **60-70%**. The pure physics configuration also remains more reliable than both data-driven models, which demonstrates that structural constraints alone already strengthen stability in this pattern-forming regime.

At $N = 100$, the advantage becomes even more visible. The data-driven networks experience only mild progress when more samples are provided, while PENCO continues to lower the error substantially. At the final time evaluation, the hybrid models outperform FNO-4D and MHNO by approximately **50 to 60 percent**. This behaviour indicates that the additional data are useful only when combined with physical guidance that keeps the dynamics aligned with the correct wavelength selection.

With $N=200$, all methods show improvement, yet the differences between learning strategies remain clear. The PENCO variants reach the lowest errors at every evaluation time and reduce the long-horizon discrepancy by a factor of **about three to four** when compared with FNO 4D. Relative to MHNO, the improvement is from **40-50 percent**. This level of stability across the entire rollout shows that PENCO delivers higher accuracy and better data efficiency, enabling it to reproduce the SH pattern formation with much stronger fidelity despite the sensitivity of this higher order system.

Table 4-3: Relative L_2 -norm errors for SH equation ($L = 15$, grid 32^3 , $\Delta t = 0.05$, $\epsilon = 0.15$)

N	Method	$0\Delta t$	$20\Delta t$	$40\Delta t$	$60\Delta t$	$80\Delta t$	$100\Delta t$
50	FNO-4d	0	0.12	0.17	0.21	0.23	0.24
50	MHNO	0	0.11	0.16	0.18	0.21	0.25
50	PENCO ($\lambda = 0.25$)	0	0.03	0.05	0.06	0.07	0.08
50	PENCO ($\lambda = 0.50$)	0	0.03	0.06	0.07	0.08	0.08
50	PENCO ($\lambda = 0.75$)	0	0.03	0.06	0.08	0.09	0.09
50	Pure Phys. ($\lambda = 1.0$)	0	0.03	0.08	0.1	0.11	0.11

100	FNO-4d	0	0.07	0.11	0.14	0.15	0.15
100	MHNO	0	0.07	0.1	0.12	0.14	0.17
100	PENCO ($\lambda = 0.25$)	0	0.02	0.04	0.05	0.06	0.07
100	PENCO ($\lambda = 0.50$)	0	0.02	0.04	0.06	0.07	0.07
100	PENCO ($\lambda = 0.75$)	0	0.02	0.05	0.07	0.08	0.09
100	Pure Phys. ($\lambda = 1.0$)	0	0.03	0.08	0.1	0.11	0.11
200	FNO-4d	0	0.05	0.09	0.13	0.16	0.18
200	MHNO	0	0.03	0.06	0.08	0.09	0.11
200	PENCO ($\lambda = 0.25$)	0	0.01	0.02	0.03	0.04	0.05
200	PENCO ($\lambda = 0.50$)	0	0.01	0.02	0.04	0.05	0.06
200	PENCO ($\lambda = 0.75$)	0	0.01	0.03	0.05	0.06	0.07
200	Pure Phys. ($\lambda = 1.0$)	0	0.03	0.08	0.1	0.11	0.11

4.1.4 Atomic-Scale Crystallization: The Phase Field Crystal Model

The Phase Field Crystal equation models crystallization at atomic resolution and provides a continuum description of periodic density fields. It captures essential physical mechanisms such as lattice formation, defect migration and long-range diffusion that governs microstructural stability. The equation combines a SH-type pattern-forming energy with a mass-conserving CH dynamics, giving rise to periodic structures that evolve through conserved fluxes [61, 62]. Within our unified formulation this behavior is obtained by activating the α_4 term, which introduces the wavelength-selective energy needed to generate a crystalline lattice.

The qualitative evolution of the crystalline patterns is illustrated in [Figure 4-10](#) and [Figure 4-11](#). All models reproduce the interior lattice, while the clearest differences appear at the boundaries where conserved flux and long range coupling control the dynamics. The data driven networks gradually lose coherence in these regions, which is consistent with the relative error behavior in [Figure 4-12](#). Both FNO-4d and MHNO show an early rise in error followed by steady growth, indicating that they do not fully capture the conserved transport and wavelength selection characteristic of the PFC system.

The hybrid PENCO model maintains stable lattice alignment across the entire domain and avoids the boundary drift observed in the data driven approaches. The error curve in [Figure 4-12](#) reflects this stability, remaining low and slowly varying throughout the rollout. The purely physics-based solution retains global consistency but lacks the refinement provided by training data. The overall behavior resembles the trends seen in the AC case, which can be attributed to the shared structure of the conserved flux operator and the similar number of update steps used during training. These common elements lead to comparable stability characteristics across both systems, while the hybrid PENCO design continues to deliver the most accurate representation of the evolving patterns.

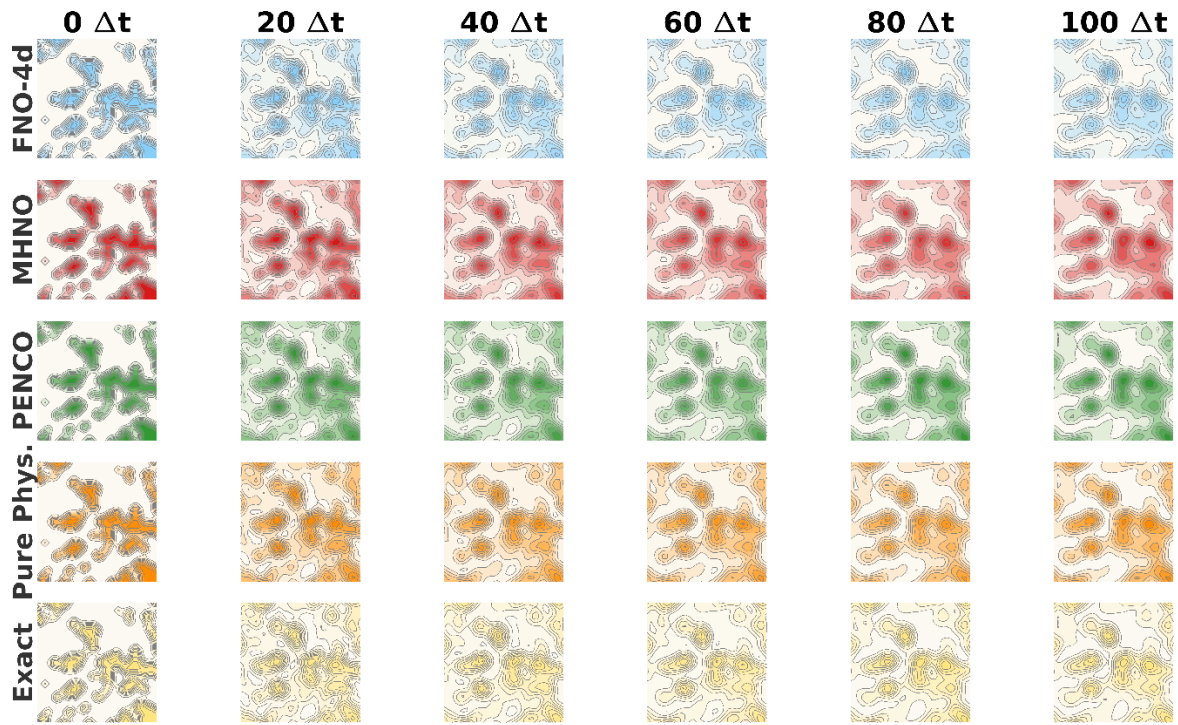


Figure 4-10: Two-dimensional contour evolution for the PFC system ($L = 10\pi$, grid 32^3 , $\Delta t = 0.01$, $\epsilon = 0.5$, $N = 200$)

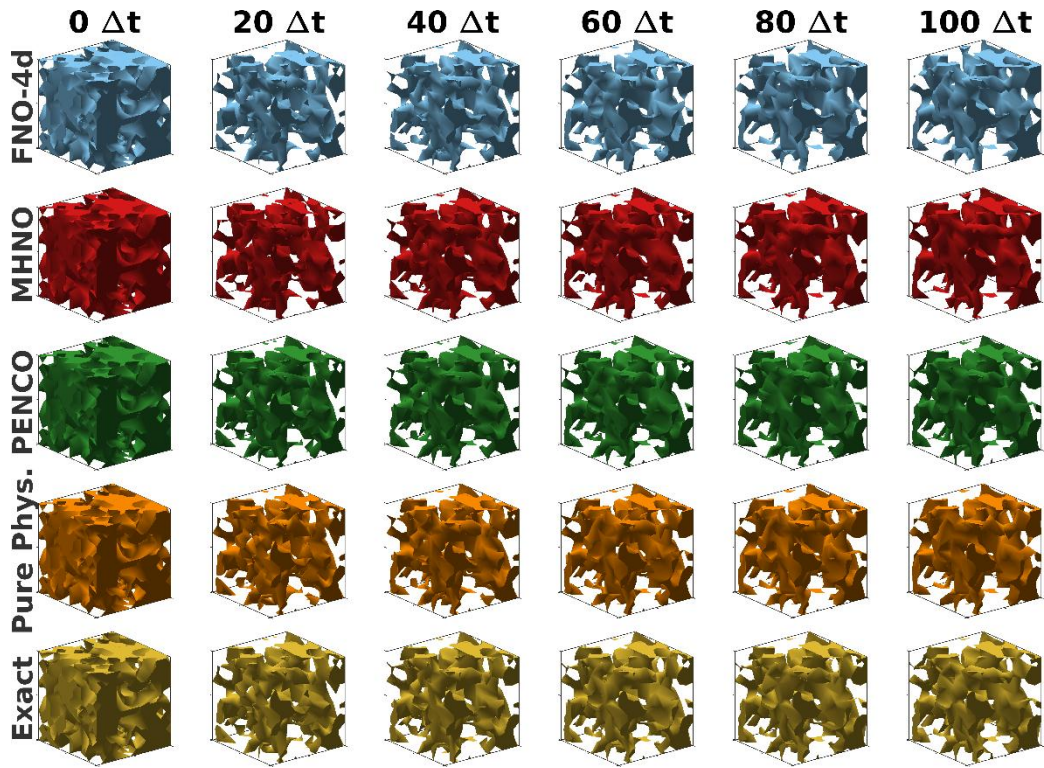


Figure 4-11: Three-dimensional crystalline morphology evolution across all models.

[Figure 4-12](#) compares the total training loss and the temporal evolution of the relative L_2 -error for all methods. The results clearly demonstrate the advantage of coupling data with physics. The hybrid Penco

configurations display smooth and steady optimization behavior, while purely data-driven and purely physics-based models show larger oscillations and slower error decay.

The relative error plots highlight a distinct contrast between learning regimes. After the initial transient, the FNO-4D and MHNO models undergo a sharp error rise, followed by a gradual stabilization at significantly higher magnitudes. This indicates unstable transient dynamics caused by the absence of explicit conservation and energy-dissipation constraints. In contrast, the PENCO variants maintain consistently low error levels across the full rollout. The inclusion of even moderate physics weighting effectively suppresses the early overshoot and prevents the runaway divergence characteristic of the purely data-based networks. The fully physics-based model also overshoots initially due to the lack of data, and its error increases gently over time, though it still outperforms purely data-driven models. PENCO achieves the lowest and most stable errors overall, highlighting its superior handling of complex conservative dynamics.

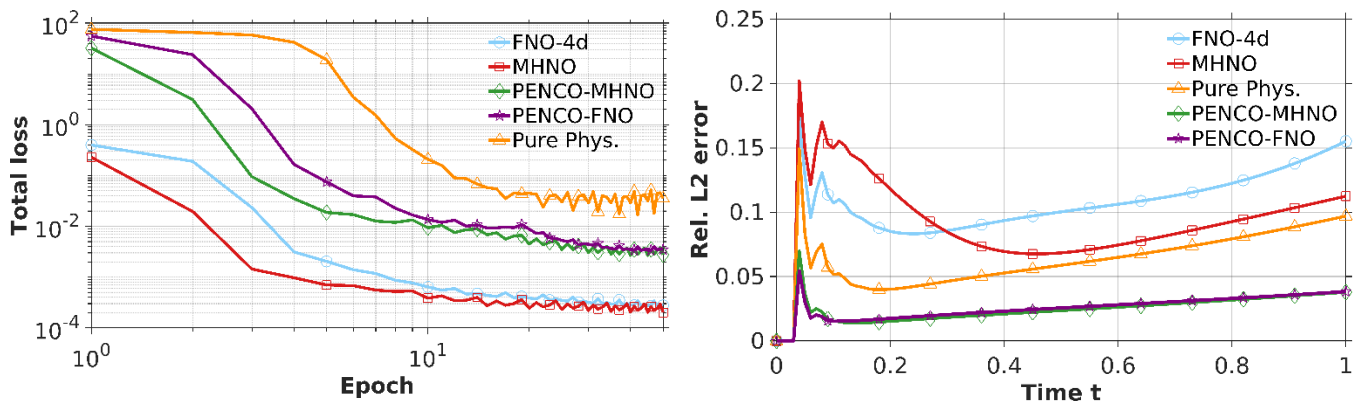


Figure 4-12: Total loss and relative error for the PFC system showing the accuracy and stability of the different models.

The results in [Table 4-4](#) show that PENCO achieves a clear accuracy advantage at every data level. For $N = 50$, the hybrid models reduce the long-horizon error by about **70–75%** compared with both data-driven baselines, demonstrating that even modest physics guidance substantially improves stability when training data are scarce.

At $N = 100$, PENCO maintains this lead, lowering the final error by roughly **65–75%** relative to the baselines. The pure-physics model also surpasses the data-driven methods, though it remains less accurate than the hybrid configurations, indicating the added benefit of data-based refinement.

For $N = 200$, all models improve with additional data, yet PENCO continues to deliver the smallest errors, achieving a **50–75%** reduction compared with the data-driven architectures. These gains indicate that the hybrid formulation retains the essential physical structure of the PFC system more effectively than either data-only or physics-only learning.

Table 4-4: Relative L_2 -norm errors for the PFC equation ($L = 10\pi$, grid 32^3 , $\Delta t = 0.01$, $\epsilon = 0.5$)

N	Method	$0\Delta t$	$20\Delta t$	$40\Delta t$	$60\Delta t$	$80\Delta t$	$100\Delta t$
50	FNO-4d	0	0.17	0.21	0.25	0.3	0.35
50	MHNO	0	0.14	0.18	0.24	0.31	0.38
50	PENCO ($\lambda = 0.25$)	0	0.04	0.05	0.07	0.08	0.1
50	PENCO ($\lambda = 0.50$)	0	0.04	0.05	0.07	0.08	0.1
50	PENCO ($\lambda = 0.75$)	0	0.04	0.05	0.07	0.08	0.1
50	Pure Phys. ($\lambda = 1.0$)	0	0.04	0.05	0.06	0.08	0.1
100	FNO-4d	0	0.09	0.11	0.14	0.18	0.24
100	MHNO	0	0.12	0.09	0.1	0.12	0.15
100	PENCO ($\lambda = 0.25$)	0	0.02	0.03	0.04	0.05	0.06
100	PENCO ($\lambda = 0.50$)	0	0.02	0.03	0.04	0.05	0.06
100	PENCO ($\lambda = 0.75$)	0	0.02	0.03	0.04	0.05	0.06
100	Pure Phys. ($\lambda = 1.0$)	0	0.04	0.05	0.06	0.08	0.1
200	FNO-4d	0	0.09	0.09	0.11	0.12	0.16
200	MHNO	0	0.12	0.07	0.07	0.09	0.11
200	PENCO ($\lambda = 0.25$)	0	0.02	0.02	0.03	0.03	0.04
200	PENCO ($\lambda = 0.50$)	0	0.01	0.02	0.03	0.03	0.04
200	PENCO ($\lambda = 0.75$)	0	0.02	0.02	0.03	0.03	0.04
200	Pure Phys. ($\lambda = 1.0$)	0	0.04	0.05	0.06	0.08	0.1

4.1.5 Thin-Film Epitaxial Growth: The Molecular Beam Epitaxy Model

The Molecular Beam Epitaxy equation models thin-film growth driven by the interplay of high-order surface diffusion and a nonlinear slope-selection flux, a mechanism central to understanding mound formation and coarsening in epitaxial systems [63, 64]. Within our unified formulation this behavior is obtained by activating the α_5 term, which introduces the characteristic fourth order smoothing and slope-dependent dynamics that make the MBE system one of the most challenging benchmarks in our study.

The MBE case reveals the clearest separation between approaches. As seen in the two- and three-dimensional evolutions in [Figure 4-13](#) and [Figure 4-14](#), the data-driven models depart quickly from the true surface dynamics, losing the correct mound geometry and coarsening behavior, while the pure-physics model remains stable but lacks fine-scale accuracy. These qualitative differences are confirmed quantitatively by [Figure 4-15](#), where FNO-4d and MHNO show a sharp early error surge and continued growth, indicating that they cannot sustain the nonlinear slope-selection mechanism of the MBE equation. In contrast, the hybrid PENCO model remains closely aligned with the reference across the entire rollout, accurately preserving both the surface morphology and boundary motion. Its relative error stays low and nearly flat, reflecting a level of stability that is difficult to achieve for an equation governed by high-order diffusion and strongly nonlinear slope-selection fluxes.

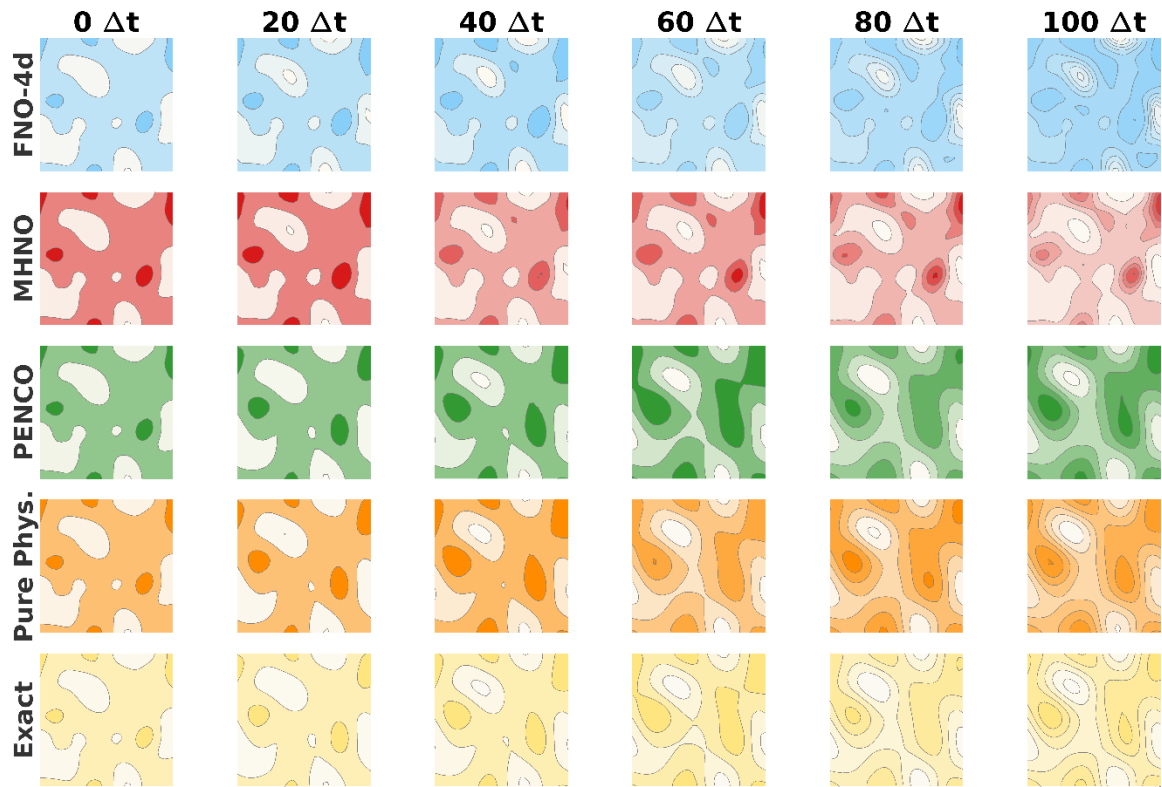


Figure 4-13: Two-dimensional contour evolution of the MBE surface field for FNO-4D, MHNO, PENCO, pure-physics, and the reference solution (32^3 grid, $\Delta t = 0.005$, $\epsilon = 0.1$, $N_t = 100$, $L = 2\pi$, $N = 200$).

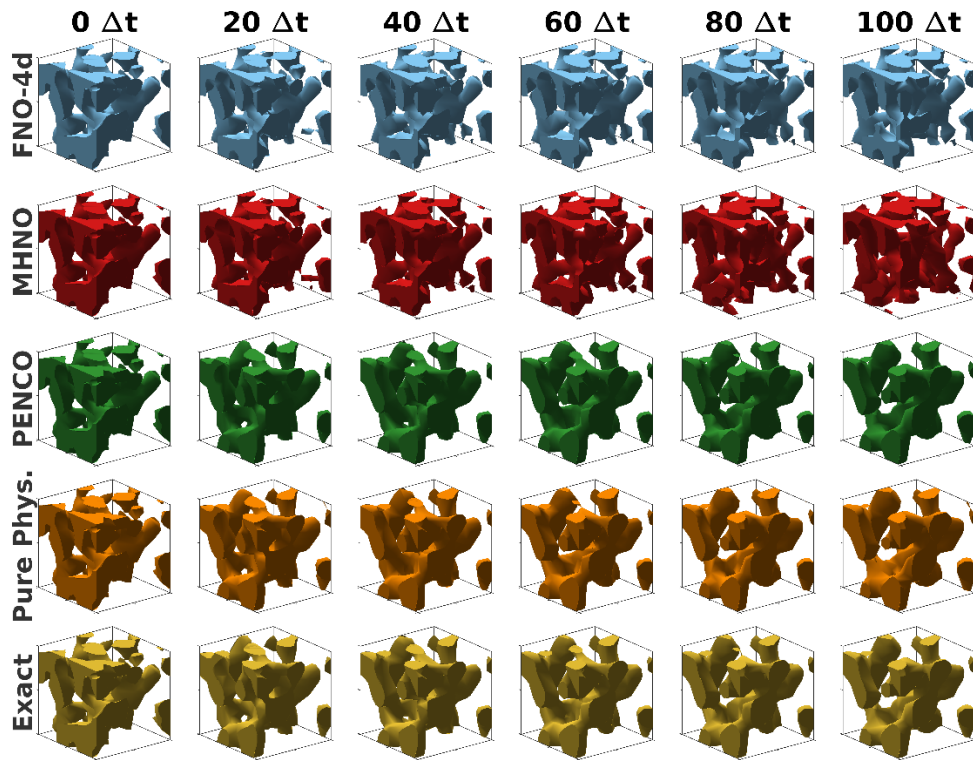


Figure 4-14: 3D phase evolution of the MBE system predicted by different models.

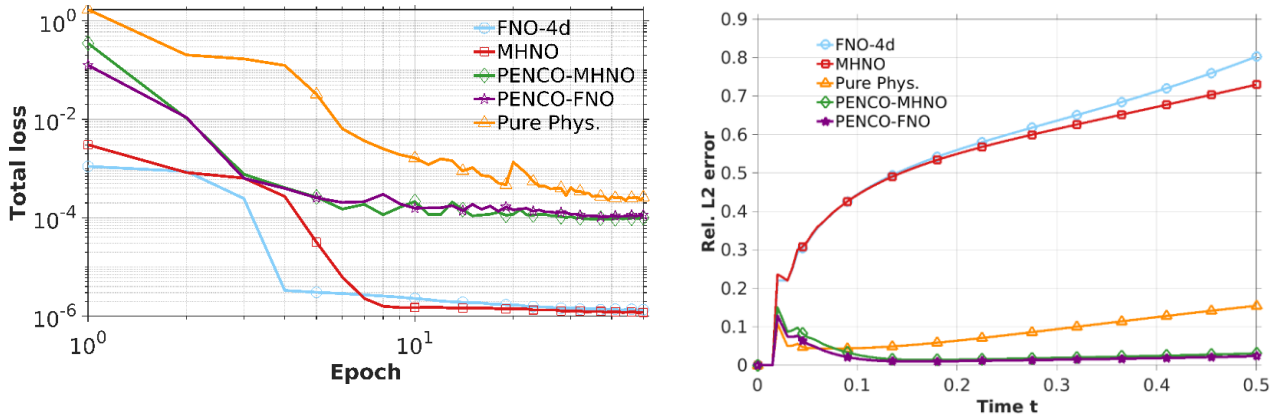


Figure 4-15: Total loss and relative L_2 -norm error for the MBE equation using different methods

The quantitative results show the steep difficulty of the MBE system for data-driven surrogates. As summarized in [Table 4-5](#), the purely data-driven models experience severe long-horizon degradation, while PENCO maintains substantially higher fidelity across all dataset sizes. With $N = 50$, the discrepancy between the approaches is dramatic. PENCO reduces the long-term error by more than **95 %** relative to FNO-4D and by approximately **70 %** relative to MHNO, demonstrating its ability to stabilize the evolution even under minimal data availability. The pure-physics model also improves significantly over the data-driven baselines but remains about **30 %** less accurate than PENCO, reflecting the importance of data-guided correction for this strongly nonlinear, high-order PDE.

For $N = 100$, the same ordering persists. PENCO lowers the final-time error by around 85 % compared with MHNO and by over **90 %** compared with FNO-4D, indicating that additional data amplify, rather than diminish, the benefit of physics-guided learning. With $N = 200$, all models improve due to increased training samples, yet PENCO still provides the clearest advantage, achieving an accuracy gain of nearly **90 %** relative to MHNO and approximately **95 %** relative to FNO-4D. The pure-physics solution remains stable throughout but continues to trail PENCO by roughly **25–30 %**, highlighting the essential role of hybrid learning in capturing both the nonlinear flux term and the high-order diffusion that govern MBE surface evolution.

Table 4-5: Relative L_2 -norm errors for MBE equation ($L = 2\pi$, grid 32^3 , $\Delta t = 0.005$, $\epsilon = 0.1$)

N	Method	$0\Delta t$	$20\Delta t$	$40\Delta t$	$60\Delta t$	$80\Delta t$	$100\Delta t$
50	FNO-4d	0	0.49	0.8	1.75	4.32	8.23
50	MHNO	0	0.33	0.45	0.54	0.61	0.66
50	PENCO ($\lambda = 0.25$)	0	0.08	0.09	0.13	0.17	0.21
50	PENCO ($\lambda = 0.50$)	0	0.06	0.08	0.11	0.15	0.18
50	PENCO ($\lambda = 0.75$)	0	0.05	0.07	0.1	0.13	0.17
50	Pure Phys. ($\lambda = 1.0$)	0	0.04	0.06	0.09	0.12	0.15
100	FNO-4d	0	0.46	0.62	0.8	1.16	1.74
100	MHNO	0	0.43	0.53	0.59	0.64	0.69
100	PENCO ($\lambda = 0.25$)	0	0.04	0.04	0.06	0.07	0.09

100	PENCO ($\lambda = 0.50$)	0	0.03	0.04	0.05	0.07	0.08
100	PENCO ($\lambda = 0.75$)	0	0.03	0.04	0.05	0.06	0.08
100	Pure Phys. ($\lambda = 1.0$)	0	0.04	0.06	0.09	0.12	0.15
200	FNO-4d	0	0.44	0.56	0.64	0.71	0.8
200	MHNO	0	0.44	0.55	0.61	0.67	0.73
200	PENCO ($\lambda = 0.25$)	0	0.03	0.01	0.02	0.02	0.03
200	PENCO ($\lambda = 0.50$)	0	0.02	0.02	0.02	0.03	0.03
200	PENCO ($\lambda = 0.75$)	0	0.02	0.02	0.02	0.03	0.04
200	Pure Phys. ($\lambda = 1.0$)	0	0.04	0.06	0.09	0.12	0.15

4.2 Out-of-Distribution (OOD) Generalization

To evaluate generalization beyond the GRF-based training distribution, we test all models on deterministic initial conditions whose geometry and spectral content differ fundamentally from the training set. For AC, CH, and SH we impose the smooth spherical initialization

$$u(\mathbf{x}, 0) = \tanh\left(\frac{R - \sqrt{x^2 + y^2 + z^2}}{\sqrt{b}\epsilon}\right), \quad (30)$$

while for the PFC system we introduce a strongly anisotropic star-shaped interface,

$$R_\theta = 10.0 + 5.0 \times \cos(6\theta), \quad u_0(\mathbf{x}) = \tanh[(R_\theta - d)/(7\epsilon)] \quad (31)$$

and for MBE we apply the torus configuration

$$u(\mathbf{x}, 0) = \tanh\left(\frac{r_0 - \sqrt{(\sqrt{x^2 + y^2} - R)^2 + z^2}}{w}\right), \quad (32)$$

where R is the major radius, r_0 is the tube radius, and w denotes the interfacial width. These geometries, shown in [Figure 4-16\(a–e\)](#), vary in curvature, interface width, and topological complexity, making prediction accuracy highly sensitive to the underlying surface shape and therefore an informative probe of OOD generalization. All comparisons use $N = 200$ and the hybrid model with $\lambda = 0.25$.

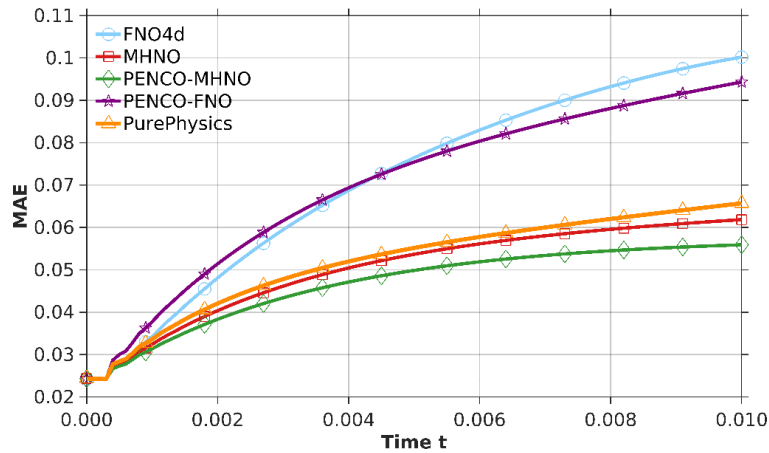
Across all PDEs and OOD configurations, FNO-4D remains the least accurate method (as shown in [Figure 4-16](#)). Its MAE consistently grows throughout the rollout and tends to rise more rapidly than the other models once the evolution departs from the GRF statistics used during training. This reflects its limited ability to adapt when the unseen initial condition introduces geometric structure, sharper or smoother interfaces, or curvature patterns not represented in the training distribution.

MHNO consistently outperforms FNO-4D across all OOD tests. Its design includes a shared spectral encoder together with time-step-specific projection and transition networks, allowing it to refine spatial features dynamically and propagate information more coherently through time. These capabilities make MHNO more resilient to unseen geometries and non-GRF interfaces. In the AC and PFC systems, MHNO even surpasses the pure-physics model because these equations rely strongly on interface regularity and periodic microstructure, which benefit from MHNO’s learned spatial refinement. In the remaining PDEs,

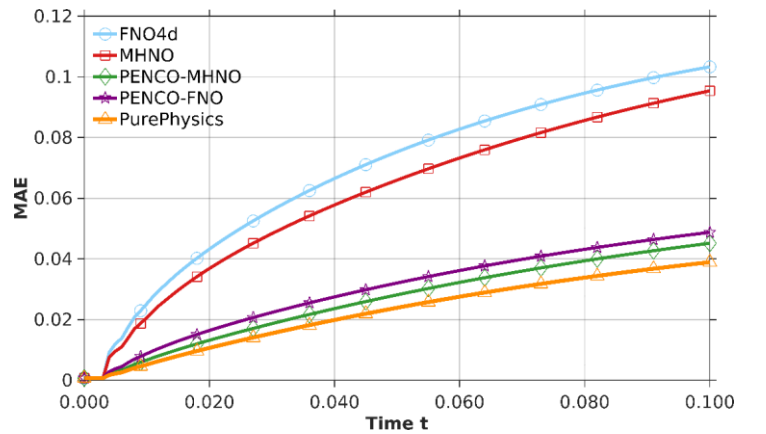
MHNO remains clearly stronger than FNO-4D, reflecting its improved ability to represent nonlinear evolution and sharper interface motion.

The hybrid PENCO models provide the strongest overall OOD generalization across four of the five systems, as observed in [Figure 4-16](#). Physics regularization removes the early overshoot characteristic of the data-only operators and stabilizes long-horizon predictions when the initial condition departs significantly from the GRF statistics. By enforcing the structural constraints of each PDE while still benefiting from data-driven refinement, PENCO produces the most reliable MAE behavior for the spherical, star, and torus tests. In CH, the pure-physics model attains slightly higher accuracy because the dynamics are dominated by strict mass conservation and curvature-driven coarsening, both fully encoded in the PDE. In the remaining systems, particularly SH, PFC, and MBE, PENCO model achieves the best performance, as the combination of physics constraints and learned spatial refinement allows it to track wavelength-selective dynamics and nonlinear flux behavior more accurately than either data-only or physics-only models.

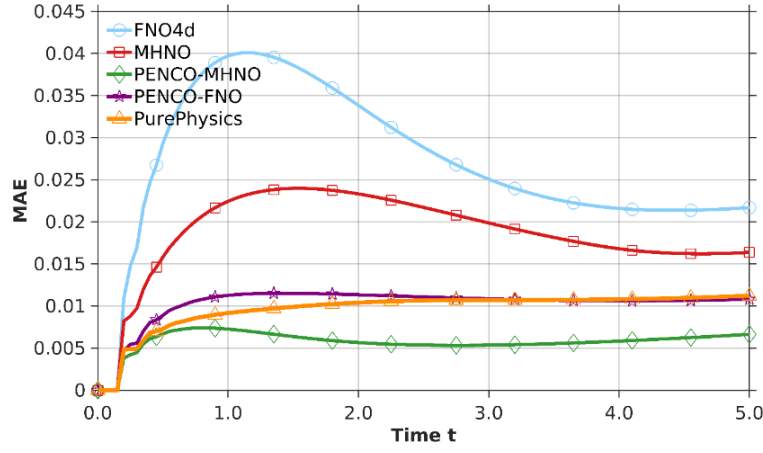
The pure-physics configuration behaves differently depending on the governing equation. It performs exceptionally well in CH, SH, and MBE, where the evolution is dominated by strict conservation laws, curvature-controlled coarsening, or slope-regulated diffusion; all of these mechanisms are fully encoded in the PDE and therefore generalize well to unseen initial conditions without needing data-driven correction. In AC and PFC, however, pure physics is matched or slightly overtaken by MHNO because these systems involve interface sharpening and periodic lattice formation that benefit from learned spatial detail not explicitly enforced by the PDE. Overall, the physics-only model remains stable in every OOD test but lacks the adaptive refinement provided by PENCO or MHNO when geometric complexity is high.



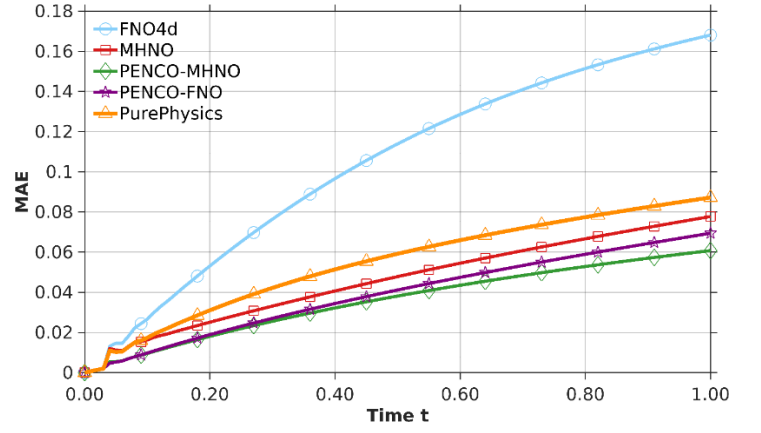
a) AC with spherical IC ($R = 0.5$, $\epsilon = 0.05$, $b = 2$)



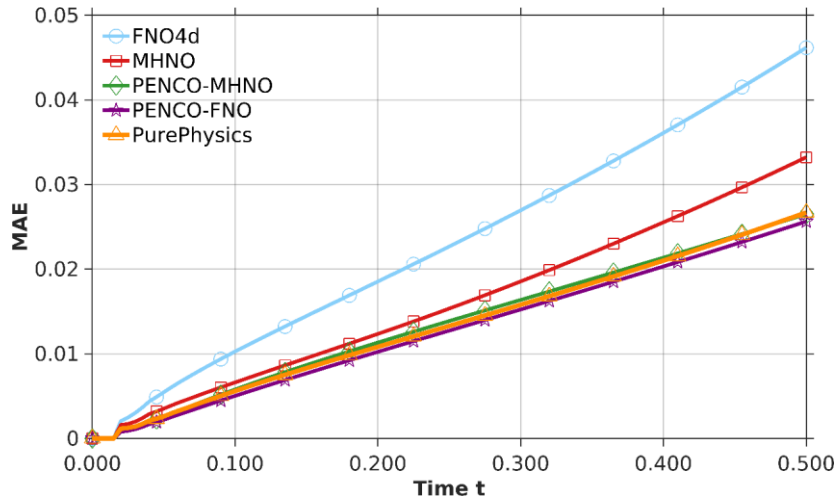
b) CH with spherical IC ($R = 0.5$, $\epsilon = 0.05$, $b = 2$)



c) SH with spherical IC ($R = 5, \epsilon = 0.15, b = 2$)



d) PFC with star-shaped IC ($\theta = \tan^{-1}(z/x), d = \sqrt{x^2 + 2y^2 + z^2}, \epsilon = 0.5$)



e) MBE with torus IC ($R = 0.5, r_0 = 0.1, w = 2\epsilon$)

Figure 4-16(a–e): Each panel shows MAE over time for all architectures (FNO-4D, MHNO, PENCO-MHNO, PENCO-FNO, physics-only), illustrating the effect of geometry-dependent shifts in curvature and interface structure on predictive accuracy.

5 Conclusion

This work introduced PENCO, a physics guided operator learning framework for nonlinear and higher order phase field systems. Beyond coupling the structure of the governing equations with data driven refinement, PENCO incorporates several key innovations in its loss design such as Gauss Lobatto collocation points that enforce symmetric and stable residuals of the partial differential equation, epoch dependent weighting schedules that smoothly shift the training focus from local scheme accuracy to global spectral stability, and a low frequency anchor term that prevents drift in the dominant Fourier modes.

Across all equations considered, PENCO provides the most stable long horizon behavior and the lowest accumulated error. The hybrid formulation consistently outperforms purely data driven models, which tend to drift once the dynamics leave the statistics of the training set, and it improves over the pure physics model by recovering fine scale features that the PDE alone cannot generate.

Furthermore, PENCO achieves these improvements while relying on a much lighter computational configuration than the original MHNO study [50], which was developed for two-dimensional settings. In our three-dimensional experiments, the spatial resolution is reduced from 64^3 to 32^3 , the operator depth from four–six layers to two, and the training horizon is reduced by a factor of ten to fifty epochs, all while preserving accuracy, stability, and robustness.

When evaluated on spherical, star shaped, and torus based initial conditions that differ strongly from the GRF distribution used for training, PENCO maintains coherent evolution and low error for every system except CH, where the pure physics model aligns slightly more closely with the reference due to its strictly conservative structure. In the remaining equations, the hybrid model achieves the highest accuracy, demonstrating that combining physical constraints with learned spatial refinement offers strong robustness to unseen geometries.

Future directions

The framework can be extended in two natural directions. First, integrating fracture and crack growth models would enable prediction of crack initiation and propagation within the same hybrid operator formulation. Second, supporting non periodic boundary conditions would allow application to more realistic geometries and multi physics settings. These developments would further expand the applicability of machine learning accelerated phase field modeling.

Acknowledgments

The authors acknowledge funding from the German Academic Exchange Service (DAAD), which provided a doctoral scholarship to Mostafa Bamdad that supported the work presented in this paper.

6 Appendix: Numerical Solver

The Fourier-spectral method is a powerful numerical approach for solving phase-field equations, offering spectral accuracy by leveraging the efficiency of the Fast Fourier Transform (FFT). Below, we describe its adaptation to three-dimensional (3D) simulations, focusing on the CH equation as a representative example.

Consider a 3D periodic domain $\Omega = [l_x, r_x] \times [l_y, r_y] \times [l_z, r_z]$, discretized into a grid of $N_x \times N_y \times N_z$, and the grid spacing is defined by $h_x = \frac{L_x}{N_x}$, $h_y = \frac{L_y}{N_y}$, $h_z = \frac{L_z}{N_z}$, with domain lengths $L_x = r_x - l_x$, $L_y = r_y - l_y$ and $L_z = r_z - l_z$. The spatial coordinates are:

$$(x_m, y_n, z_l) = (l_x + mh_x, l_y + nh_y, l_z + lh_z), \quad (0 \leq m \leq N_x, 0 \leq n \leq N_y, 0 \leq l \leq N_z) \quad (33)$$

The 3D Discrete Fourier Transform (DFT) of a time-varying field $\phi(x, y, z, t)$ at time step $t_k = k\Delta t$:

$$\widehat{\phi_k^{p,q,r}} = \sum_{m=1}^{N_x} \sum_{n=1}^{N_y} \sum_{l=1}^{N_z} \phi_k^{m,n,l} e^{-i(\xi_p x_m + \eta_q y_n + \zeta_r z_l)} \quad (34)$$

Where the wavenumbers $\xi_p = \frac{2\pi p}{L_x}$, $\eta_q = \frac{2\pi q}{L_y}$, $\zeta_r = \frac{2\pi r}{L_z}$, are indexed by integers p, q, r in the ranges:

$$-\frac{N_x}{2} + 1 \leq p \leq \frac{N_x}{2}, \quad -\frac{N_y}{2} + 1 \leq q \leq \frac{N_y}{2}, \quad -\frac{N_z}{2} + 1 \leq r \leq \frac{N_z}{2} \quad (35)$$

The inverse discrete Fourier transform (IDFT) bridges Fourier space and physical space, synthesizing the field $\phi(x, y, z, t_k)$ from its spectral coefficients. At each time step t_k the solution is reconstructed by summing contributions from all Fourier modes:

$$\phi_k^{m,n,l} = \frac{1}{N_x N_y N_z} \sum_{p=-N_x/2+1}^{N_x/2} \sum_{q=-N_y/2+1}^{N_y/2} \sum_{r=-N_z/2+1}^{N_z/2} \widehat{\phi_k^{p,q,r}} e^{i(\xi_p x_m + \eta_q y_n + \zeta_r z_l)} \quad (36)$$

This operation combines all wavenumber modes (ξ_p, η_q, ζ_r) , weighted by their amplitudes $\widehat{\phi_k^{p,q,r}}$, to reproduce the field's spatial structure.

Derivatives are computed with spectral accuracy by leveraging the Fourier transform's unique properties. In Fourier space, differentiation simplifies to multiplication by wavenumbers:

$$\partial\phi/\partial x \rightarrow^{(DFT)} i\xi_p \widehat{\phi^{p,q,r}}, \quad \partial\phi/\partial y \rightarrow^{(DFT)} i\eta_q \widehat{\phi^{p,q,r}}, \quad \partial\phi/\partial z \rightarrow^{(DFT)} i\zeta_r \widehat{\phi^{p,q,r}} \quad (37)$$

The Laplacian acts as a low-pass filter, damping high-wavenumber modes more strongly due to the quadratic dependence on (ξ_p, η_q, ζ_r) :

$$\Delta\phi \rightarrow^{(DFT)} -(\xi_p^2 + \eta_q^2 + \zeta_r^2) \widehat{\phi^{p,q,r}} \quad (38)$$

The CH equation describes phase separation dynamics and is solved using a linearly stabilized splitting scheme. The time-discretized form on a 3D grid x_m, y_n, z_l in physical space is:

$$\frac{\phi_k^{m,n,l} - \phi_{k-1}^{m,n,l}}{\Delta t} = \Delta \left(2\phi_k^{m,n,l} - \epsilon^2 (\Delta\phi_k)^{m,n,l} + f(\phi_{k-1}^{m,n,l}) \right), \quad (39)$$

Where $f(\phi) = \phi^3 - 3\phi$ is the nonlinear term, and ϵ controls interfacial energy. Transforming to Fourier space yields:

$$\frac{\widehat{\phi}_k^{p,q,r} - \widehat{\phi}_{k-1}^{p,q,r}}{\Delta t} = -(\xi_p^2 + \eta_q^2 + \zeta_r^2) \left(2\widehat{\phi}_k^{p,q,r} + \epsilon^2(\xi_p^2 + \eta_q^2 + \zeta_r^2)\widehat{\phi}_k^{p,q,r} + \widehat{f}_{k-1}^{p,q,r} \right), \quad (40)$$

where ξ_p, η_q and ζ_r are wavenumbers in x, y, z directions. Solving for $\widehat{\phi}_k^{p,q,r}$ gives the update rule:

$$\widehat{\phi}_k^{p,q,r} = \frac{\widehat{\phi}_{k-1}^{p,q,r} - \Delta t(\xi_p^2 + \eta_q^2 + \zeta_r^2)\widehat{f}_{k-1}^{p,q,r}}{1 + \Delta t \left[2(\xi_p^2 + \eta_q^2 + \zeta_r^2) + \epsilon^2(\xi_p^2 + \eta_q^2 + \zeta_r^2)^2 \right]} \quad (41)$$

The physical-space solution is reconstructed via the inverse DFT:

$$\phi_k^{m,n,l} = \frac{1}{N_x N_y N_z} \sum_{p=-N_x/2+1}^{N_x/2} \sum_{q=-N_y/2+1}^{N_y/2} \sum_{r=-N_z/2+1}^{N_z/2} \widehat{\phi}_k^{p,q,r} e^{i(\xi_p x_m + \eta_q y_n + \zeta_r z_l)} \quad (42)$$

This method ensures high-fidelity simulations of phase-field dynamics in 3D. For further implementation details, see [7, 50].

Supplementary Information

S1 Supplementary Tables

S1.1 Summary of notation

Table S1.1 provides a compact reference for all mathematical symbols and model components appearing in the paper, grouped by their functional roles.

Table S1.1. Notation overview for fields, operators, and model components

Symbol	Description
<u>Domains, Coordinates, Fields</u>	
$\Omega \subset R^3, t \in [0, T], \mathbf{x} = (x, y, z)$	Periodic spatial domain, Time interval, Spatial coordinate
$u(x, t), u^n \approx u(\mathbf{x}, t_n)$	Continuous field and its discrete-time representation
$\hat{u}^{n+1}, \Delta t$	Predicted next-step field, and uniform time step
<u>Differential Operators</u>	
$\nabla u, \nabla^2 u, \nabla^4 u$	Gradient of u , Laplacian, Biharmonic operator
$\mathcal{R}, \mathcal{D}, \mathcal{M}, L(u), \mathcal{N}(u)$	PDE residual, evolution operator, mobility operator, linear and nonlinear part of the PDE
<u>Neural Operators</u>	
$\mathcal{G}_\theta, a(\mathbf{x})$	Learned solution operator and its input initial condition
$v_\tau, \mathcal{W}_\tau, K_\tau$	Latent feature, local linear transform, spectral convolution at layer τ
$\mathcal{P}, \mathcal{Q}, R_\tau(\mathbf{k}), \mathbf{k} = (k_x, k_y, k_z)$	Lifting & projection networks, spectral filter, wavenumber vector
<u>MHNO-specific symbols</u>	

$\mathcal{Q}_n, \mathcal{H}_n, v_a(x)$	Projection head, transition head, and shared spatial latent feature
PENCO	
$\tau_{1,2} = \frac{1}{2} \pm \frac{1}{2\sqrt{5}}, R_\tau, \tilde{R}_\tau$	Gauss–Lobatto nodes, collocation residual, and normalized residual
$\dot{u}^n = \frac{\hat{u}^{n+1} - u^n}{\Delta t}, u_\tau = (1 - \tau)u^n + \tau\hat{u}^{n+1}$	Predicted time derivative and interpolated midpoint state
$E[u], F(u), \epsilon$	Free-energy functional, bulk potential, interfacial thickness
$u_{SI}^{n+1}, \mathcal{P}_{low-k}(u), \lambda, \alpha$	Semi-implicit update, low-frequency spectral projection, and physics–data weighting/loss balance factors
PENCO-FNO, PENCO-MHNO	FNO and MHNO architectures augmented with PENCO physics constraints

S1.2 Summary of hyperparameters

Table S1.2 summarizes the hyperparameters used across all neural operator models considered in this study, including FNO, MHNO, PENCO-FNO, PENCO-MHNO, and the pure-physics model. The table reports the number of training epochs, dataset sizes, learning rates, number of layers, model widths and depths, and the number of retained Fourier modes.

The temporal hyperparameters T_{in} and T_{out} control how the models process time. The first sets how many past solution states are provided as input, and the second determines how many future states are predicted in each forward pass.

Table S1.2: Summary of neural operator hyperparameters used for all experiments

Problems	Epochs	N_{train}	N_{test}	$T_{\text{in}}, T_{\text{out}}$	Lr	W_Q	W_H	M	W	N_I	N_Q	N_H
AC	50	50,100,200	50	4, 1	0.001	10	10	10	10	2	2	2
CH	50	-	-	-	0.001	10	10	10	10	2	2	2
SH	150	-	-	-	0.001	10	10	10	10	2	2	2
PFC	50	-	-	-	0.001	10	10	10	10	2	2	2
MBE	50	-	-	-	0.0005	11	11	10	10	2	2	2

S1.3 Summary of Computational Performance Metrics

Supplementary table S1.3 details the computational performance of our models, reporting for each governing equation the discretized domain resolution, the total number of dataset samples, the total time required for dataset generation, the training duration for datasets of 50, 100, and 200 samples, and the inference time for a single temporal rollout ($N_t = 100$, using the PENCO–MHNO model with $\lambda = 0.25$).

Table S1.3. Computational performance metrics for the evaluated equations

Examples	Resolution	Samples	Dataset (s)	Training (s)			Inference (s)		
				50	100	200	50	100	200
AC	32×32×32	250	272.5	13.6	35.2	61.7	0.22	0.29	0.19
CH	"	"	246.5	104.7	164.6	258.1	0.37	0.26	0.22
SH	"	"	270	64.0	112.4	196.6	0.27	0.42	0.41
PFC	"	"	257.8	39.7	83.5	159.0	0.30	0.36	0.31
MBE	"	"	315.4	185.7	351.8	641.6	0.4	0.35	0.31

S2 Supplementary Result

This three-dimensional box plot (Figure S6-1) summarizes the distribution of final time relative L_2 errors across all equations, with the horizontal axes indexing the different operator architectures and training set sizes and the vertical axis showing the error magnitude. Each box aggregates results over the benchmark problems, so the median, interquartile range, and whiskers provide a compact view of how accuracy and variability change with method choice and data availability.

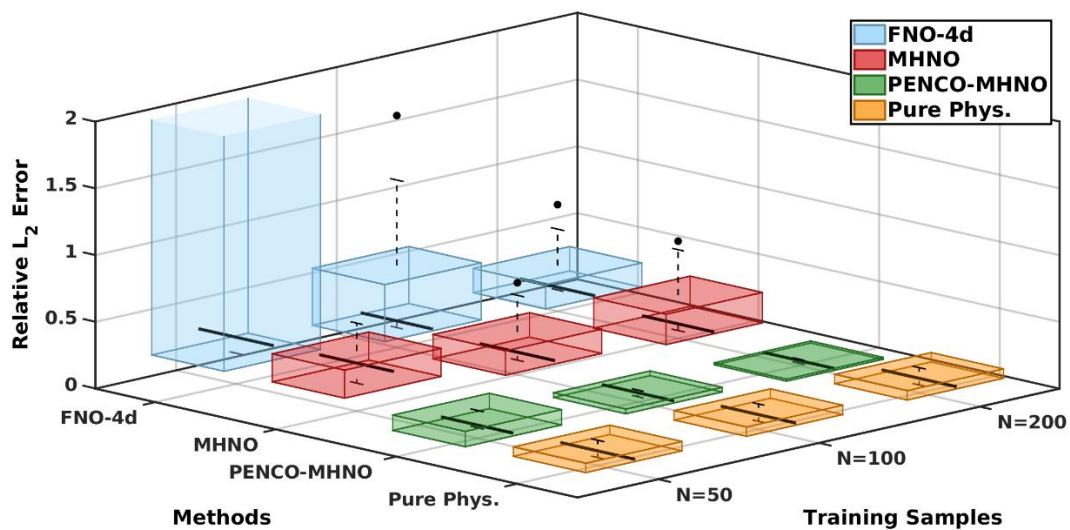


Figure S6-1: 3D box plot illustrating accuracy and variability of each operator at the final rollout time for multiple training-set sizes.

7 References

- [1] W. A. Strauss. "Partial differential equations: An introduction". In: *John Wiley & Sons* (2007).

- [2] C. L. Fefferman, J. C. Robinson, J. L. R. Diez, and J. L. Rodrigo. "Partial differential equations in fluid mechanics". In: *Cambridge University Press* 452-(2018). doi: <https://doi.org/10.1017/9781108610575>.
- [3] E. Deniz, A. Rashid, O. Hasan, and S. Tahar, "On the formalization of the heat conduction problem in HOL". In *Springer: International Conference on Intelligent Computer Mathematics* (2022), pp. 21-37, doi: https://doi.org/10.1007/978-3-031-16681-5_2.
- [4] A. Öchsner. "Partial differential equations of classical structural members: a consistent approach". In: *Springer Nature* (2019). doi: <https://doi.org/10.1007/978-3-030-35311-7>.
- [5] I. Steinbach and H. Salama. "Lectures on Phase Field". In: *Springer Nature* (2023). doi: <https://doi.org/10.1007/978-3-031-21171-3>.
- [6] H. Gomez and K. G. van der Zee. "Computational phase-field modeling". In: *Encyclopedia of computational mechanics* (2017), doi: <https://doi.org/10.1002/9781119176817.ecm2118>.
- [7] S. Yoon *et al.* "Fourier-spectral method for the phase-field equations". In: *Mathematics* 8-8 (2020), p. 1385, doi: <https://doi.org/10.3390/math8081385>.
- [8] X. Zhuang, S. Zhou, G. Huynh, P. Areias, and T. Rabczuk. "Phase field modeling and computer implementation: A review". In: *Engineering Fracture Mechanics* 262-(2022), p. 108234, doi: <https://doi.org/10.1016/j.engfracmech.2022.108234>.
- [9] Y. Gong *et al.* "A phase-field study on thermo-mechanical coupled damage evolution and failure mechanisms of sintered silver interconnections". In: *Engineering Fracture Mechanics* 320-(2025), p. 111039, doi: <https://doi.org/10.1016/j.engfracmech.2025.111039>.
- [10] P. Kumar, P. Steinmann, and J. Mergheim. "A graded interphase enhanced phase-field approach for modeling fracture in polymer composites". In: *Forces in Mechanics* 9-(2022), p. 100135, doi: <https://doi.org/10.1016/j.finmec.2022.100135>.
- [11] K. Wang *et al.* "Recent research progress on the phase-field model of microstructural evolution during metal solidification". In: *International Journal of Minerals, Metallurgy and Materials* 30-11 (2023), pp. 2095-2111, doi: <https://doi.org/10.1007/s12613-023-2710-x>.
- [12] D. Tournet, H. Liu, and J. LLorca. "Phase-field modeling of microstructure evolution: Recent applications, perspectives and challenges". In: *Progress in Materials Science* 123-(2022), p. 100810, doi: <https://doi.org/10.1016/j.pmatsci.2021.100810>.

- [13] L. Chen *et al.* "Phase separation behavior of polymer modified asphalt by molecular dynamics and phase field method: A Review". In: *Advanced Industrial and Engineering Polymer Research* (2024), doi: <https://doi.org/10.1016/j.aiepr.2024.12.002>.
- [14] S. Ham *et al.* "An explicit adaptive finite difference method for the Cahn–Hilliard equation". In: *Journal of Nonlinear Science* 32-6 (2022), p. 80, doi: <https://doi.org/10.1007/s00332-022-09844-3>.
- [15] N. Valizadeh, X. Zhuang, and T. Rabczuk. "A monolithic finite element method for phase-field modeling of fully Eulerian fluid–structure interaction". In: *Computer Methods in Applied Mechanics and Engineering* 435-(2025), p. 117618, doi: <https://doi.org/10.1016/j.cma.2024.117618>.
- [16] Q. Pan, Y. Huang, T. Rabczuk, and X. Yang. "The subdivision-based IGA-EIEQ numerical scheme for the Navier–Stokes equations coupled with Cahn–Hilliard phase-field model of two-phase incompressible flow on complex curved surfaces". In: *Computer Methods in Applied Mechanics and Engineering* 424-(2024), p. 116901, doi: <https://doi.org/10.1016/j.cma.2024.116901>.
- [17] E. A. Barros de Moraes, M. Zayernouri, and M. M. Meerschaert. "An integrated sensitivity-uncertainty quantification framework for stochastic phase-field modeling of material damage". In: *International Journal for Numerical Methods in Engineering* 122-5 (2021), pp. 1352-1377, doi: <https://doi.org/10.1002/nme.6581>.
- [18] D. Montes de Oca Zapiain, J. A. Stewart, and R. Dingreville. "Accelerating phase-field-based microstructure evolution predictions via surrogate models trained by machine learning methods". In: *npj Computational Materials* 7-1 (2021), p. 3, doi: <https://doi.org/10.1038/s41524-020-00471-8>.
- [19] C. Hu, S. Martin, and R. Dingreville. "Accelerating phase-field predictions via recurrent neural networks learning the microstructure evolution in latent space". In: *Computer Methods in Applied Mechanics and Engineering* 397-(2022), p. 115128, doi: <https://doi.org/10.1016/j.cma.2022.115128>.
- [20] A. Chakraborty, C. Anitescu, X. Zhuang, and T. Rabczuk. "Domain adaptation based transfer learning approach for solving PDEs on complex geometries". In: *Engineering with Computers* 38-5 (2022), pp. 4569-4588, doi: <https://doi.org/10.1007/s00366-022-01661-2>.
- [21] C. Bonneville *et al.* "Accelerating phase field simulations through a hybrid adaptive Fourier neural operator with U-net backbone". In: *npj Computational Materials* 11-1 (2025), p. 14, doi: <https://doi.org/10.1038/s41524-024-01488-z>.

- [22] D. Ciesielski, Y. Li, S. Hu, E. King, J. Corbey, and P. Stinis. "Deep operator network surrogate for phase-field modeling of metal grain growth during solidification". In: *Computational Materials Science* 246- (2025), p. 113417, doi: <https://doi.org/10.1016/j.commatsci.2024.113417>.
- [23] P. K. Jha. "From Theory to Application: A Practical Introduction to Neural Operators in Scientific Computing". In: *arXiv preprint arXiv:2503.05598* (2025), doi: <https://doi.org/10.48550/arXiv.2503.05598>.
- [24] N. Kovachki *et al.* "Neural operator: Learning maps between function spaces with applications to pdes". In: *Journal of Machine Learning Research* 24-89 (2023), pp. 1-97, doi: <https://dl.acm.org/doi/10.5555/3648699.3648788>.
- [25] M. Raissi, P. Perdikaris, N. Ahmadi, and G. E. Karniadakis. "Physics-informed neural networks and extensions". In: *arXiv preprint arXiv:2408.16806* (2024), doi: <https://doi.org/10.48550/arXiv.2408.16806>.
- [26] B. Hao, U. Braga-Neto, C. Liu, L. Wang, and M. Zhong. "Structure preserving PINN for solving time dependent PDEs with periodic boundary". In: *arXiv preprint arXiv:2404.16189* (2024), doi: <https://doi.org/10.48550/arXiv.2404.16189>.
- [27] S. Monaco and D. Apletti. "Training physics-informed neural networks: One learning to rule them all?". In: *Results in Engineering* 18-(2023), p. 101023, doi: <https://doi.org/10.1016/j.rineng.2023.101023>.
- [28] S. Cuomo, V. S. Di Cola, F. Giampaolo, G. Rozza, M. Raissi, and F. Piccialli. "Scientific Machine Learning Through Physics-Informed Neural Networks: Where we are and What's Next". In: *Journal of Scientific Computing* 92-3 (2022), p. 88, doi: <https://doi.org/10.1007/s10915-022-01939-z>.
- [29] M. Raissi, P. Perdikaris, and G. E. Karniadakis. "Physics informed deep learning (part i): Data-driven solutions of nonlinear partial differential equations". In: *arXiv preprint arXiv:1711.10561* (2017), doi: <https://doi.org/10.48550/arXiv.1711.10561>.
- [30] Z. Li *et al.* "Physics-informed neural operator for learning partial differential equations". In: *ACM/JMS Journal of Data Science* 1-3 (2024), pp. 1-27, doi: <https://doi.org/10.48550/arXiv.2111.03794>.
- [31] W. Li, M. Z. Bazant, and J. Zhu. "Phase-Field DeepONet: Physics-informed deep operator neural network for fast simulations of pattern formation governed by gradient flows of free-energy functionals". In:

Computer Methods in Applied Mechanics and Engineering 416-(2023), p. 116299, doi: <https://doi.org/10.1016/j.cma.2023.116299>.

- [32] S. G. Rosofsky, H. Al Majed, and E. A. Huerta. "Applications of physics informed neural operators". In: *Machine Learning: Science and Technology* 4-2 (2023), p. 025022, doi: <https://doi.org/10.48550/arXiv.2203.12634>.
- [33] G. E. Karniadakis, I. G. Kevrekidis, L. Lu, P. Perdikaris, S. Wang, and L. Yang. "Physics-informed machine learning". In: *Nature Reviews Physics* 3-6 (2021), pp. 422-440, doi: <https://doi.org/10.1038/s42254-021-00314-5>.
- [34] G. Gangmei, S. Rana, B. Rolfe, K. Mitra, and S. Bhattacharyya. "Learning coupled Allen-Cahn and Cahn-Hilliard phase-field equations using Physics-informed neural operator (PINO)". In: (2025). [Online]. Available: https://ai-2-ase.github.io/papers/46_Gangmei.pdf.
- [35] Z. Li *et al.* "Fourier neural operator for parametric partial differential equations". In: *arXiv preprint arXiv:2010.08895* (2020), doi: <https://doi.org/10.48550/arXiv.2010.08895>.
- [36] L. Lu, P. Jin, and G. E. Karniadakis. "Deeponet: Learning nonlinear operators for identifying differential equations based on the universal approximation theorem of operators". In: *arXiv preprint arXiv:1910.03193* (2019), doi: <https://doi.org/10.48550/arXiv.1910.03193>.
- [37] Z. Li *et al.* "Neural operator: Graph kernel network for partial differential equations". In: *arXiv preprint arXiv:2003.03485* (2020), doi: <https://doi.org/10.48550/arXiv.2003.03485>.
- [38] V. Oommen, K. Shukla, S. Goswami, R. Dingreville, and G. E. Karniadakis. "Learning two-phase microstructure evolution using neural operators and autoencoder architectures". In: *npj Computational Materials* 8-1 (2022), p. 190, doi: <https://doi.org/10.1038/s41524-022-00876-7>.
- [39] L. H. Rieger, K. Zelič, I. Mele, T. Kutrašnik, and A. Bhowmik. "Setting the standard for machine learning in phase field prediction: a benchmark dataset and baseline metrics". In: *Scientific Data* 11-1 (2024), p. 1275, doi: <https://doi.org/10.1038/s41597-024-04128-9>.
- [40] M. Reichstein *et al.* "Deep learning and process understanding for data-driven Earth system science". In: *Nature* 566-7743 (2019), pp. 195-204, doi: <https://doi.org/10.1038/s41586-019-0912-1>.
- [41] A. Hasan, J. M. Pereira, R. Ravier, S. Farsiu, and V. Tarokh, "Learning Partial Differential Equations From Data Using Neural Networks". *ICASSP 2020 - 2020 IEEE International Conference on Acoustics, Speech and*

Signal Processing (ICASSP) 4-8 May 2020 (2020), pp. 3962-3966, doi: <https://ieeexplore.ieee.org/document/9053750>.

- [42] M. S. Eshaghi, M. Bamdad, C. Anitescu, Y. Wang, X. Zhuang, and T. Rabczuk. "Applications of scientific machine learning for the analysis of functionally graded porous beams". In: *Neurocomputing* 619-(2025), p. 129119, doi: <https://doi.org/10.1016/j.neucom.2024.129119>.
- [43] N. Chen, R. Ma, A. Chen, and C. Cui. "PC-PINNs: Physics-informed neural networks for solving the phase-field model of pitting corrosion". In: *CRC Press* (2024), pp. 244-252. doi: <https://doi.org/10.1201/9781003483755-25>.
- [44] S. Goswami, A. Bora, Y. Yu, and G. E. Karniadakis. "Physics-Informed Deep Neural Operator Networks". Cham: In: *Springer International Publishing* (2023), pp. 219-254. doi: https://doi.org/10.1007/978-3-031-36644-4_6.
- [45] A. Krishnapriyan, A. Gholami, S. Zhe, R. Kirby, and M. W. Mahoney. "Characterizing possible failure modes in physics-informed neural networks". In: *Advances in neural information processing systems* 34-(2021), pp. 26548-26560, doi: <https://doi.org/10.48550/arXiv.2109.01050>.
- [46] W. Zhang, W. Suo, J. Song, and W. Cao. "Physics Informed Neural Networks (PINNs) as intelligent computing technique for solving partial differential equations: Limitation and Future prospects". In: *arXiv preprint arXiv:2411.18240* (2024), doi: <https://doi.org/10.48550/arXiv.2411.18240>.
- [47] N. Chen, C. Cui, R. Ma, A. Chen, and S. Wang. "Sharp-PINNs: staggered hard-constrained physics-informed neural networks for phase field modelling of corrosion". In: *arXiv preprint arXiv:2502.11942* (2025), doi: <https://doi.org/10.48550/arXiv.2502.11942>.
- [48] B. Gao, R. Yao, and Y. Li. "Physics-informed neural networks with adaptive loss weighting algorithm for solving partial differential equations". In: *Computers & Mathematics with Applications* 181-(2025), pp. 216-227, doi: <https://doi.org/10.1016/j.camwa.2025.01.007>.
- [49] M. S. Eshaghi, C. Anitescu, M. Thombre, Y. Wang, X. Zhuang, and T. Rabczuk. "Variational Physics-informed Neural Operator (VINO) for solving partial differential equations". In: *Computer Methods in Applied Mechanics and Engineering* 437-(2025), p. 117785, doi: <https://doi.org/10.1016/j.cma.2025.117785>.

- [50] M. S. Eshaghi, N. Valizadeh, C. Anitescu, Y. Wang, X. Zhuang, and T. Rabczuk. "Multi-Head Neural Operator for Modelling Interfacial Dynamics". In: *arXiv preprint arXiv:2507.17763* (2025), doi: <https://doi.org/10.48550/arXiv.2507.17763>.
- [51] S. Goswami, A. Bora, Y. Yu, and G. E. Karniadakis, "Physics-Informed Deep Neural Operator Networks," in *Machine Learning in Modeling and Simulation: Methods and Applications*, vol. . Cham: Springer International Publishing, 2023, pp. 219-254.
- [52] H. Montazer Hojjat, S. Kozinov, and D. Balzani. "An a priori irreversible phase-field formulation for ductile fracture at finite strains based on the Allen–Cahn theory: a variational approach and FE-implementation". In: *Archive of Applied Mechanics* 94-2 (2024), pp. 365-390, doi: 10.1007/s00419-023-02527-9.
- [53] M. Sohaib, K. M. Furati, and A. Shah. "Space fractional Allen–Cahn equation and its applications in phase separation: A numerical study". In: *Communications in Nonlinear Science and Numerical Simulation* 137- (2024), p. 108173, doi: <https://doi.org/10.1016/j.cnsns.2024.108173>.
- [54] A. Galfré, X. Huang, F. Couenne, and C. Cogné. "The phase field method—From fundamentals to practical applications in crystal growth". In: *Journal of Crystal Growth* 620-(2023), p. 127334, doi: <https://doi.org/10.1016/j.jcrysgro.2023.127334>.
- [55] W. Wu, Y. Lin, Y. Hu, Z. He, and Y. Yang. "Phase-field modelling for degradation/failure research in lithium battery: Progress and prospects". In: *Journal of Energy Chemistry* 102-(2025), pp. 628-650, doi: <https://doi.org/10.1016/j.jechem.2024.11.030>.
- [56] S. Ding, Y. Li, Z. Lin, and Y. Yan. "Well-posedness of Navier-Stokes/Cahn-Hilliard equations modeling the dynamics of contact line in a channel". In: *arXiv e-prints* (2023), p. arXiv: 2312.17520, doi: <https://doi.org/10.48550/arXiv.2312.17520>.
- [57] N. Kühn, M. Hinze, and T. Rung. "Cahn-Hilliard Navier-Stokes simulations for marine free-surface flows". In: *Experimental and Computational Multiphase Flow* 4-3 (2022), pp. 274-290, doi: 10.1007/s42757-020-0101-3.
- [58] M. Dai, E. Feireisl, E. Rocca, G. Schimperna, and M. E. Schonbek. "Analysis of a diffuse interface model of multispecies tumor growth". In: *Nonlinearity* 30-4 (2017), p. 1639, doi: <https://doi.org/10.1088/1361-6544/aa6063>.

- [59] L. Shen, F. Denner, N. Morgan, B. van Wachem, and D. Dini. "Transient structures in rupturing thin films: Marangoni-induced symmetry-breaking pattern formation in viscous fluids". In: *Science advances* 6-28 (2020), p. eabb0597, doi: <https://doi.org/10.1126/sciadv.abb0597>.
- [60] F. Hummel, S. Jelbart, and C. Kuehn. "Geometric blow-up of a dynamic Turing instability in the Swift-Hohenberg equation". In: *Journal of Differential Equations* 427-(2025), pp. 219-309, doi: <https://doi.org/10.1016/j.jde.2025.01.036>.
- [61] M. Punke and M. Salvalaglio. "Hybrid-PFC: Coupling the phase-field crystal model and its amplitude-equation formulation". In: *Computer Methods in Applied Mechanics and Engineering* 436-(2025), p. 117719, doi: <https://doi.org/10.48550/arXiv.2407.17283>.
- [62] D. Burns, N. Provatas, and M. Grant. "Phase field crystal models with applications to laser deposition: A review". In: *Structural Dynamics* 11-1 (2024), doi: <https://doi.org/10.1063/4.0000226>.